Gottfried Wilhelm Leibniz Universität Hannover
Fakultät für Mathematik und Physik

Scaling high-precision spectroscopy in Yb^+-ions to Coulomb crystals for tests of local Lorentz invariance

Skalierung von Hochpräzisionsspektroskopie an Yb^+-Ionen auf Coulomb-Kristalle zur Überprüfung lokaler Lorentzinvarianz

Kai Christian Grensemann
geboren am 8. August 1997 in Norden, Deutschland

Wissenschaftliche Arbeit zur Erlangung des Grades
Master of Science (M.Sc.)
am QUEST-Institut der Physikalisch-Technischen Bundesanstalt

Erstprüferin: Prof. Dr. Tanja E. Mehlstäubler
Zweitprüfer: Priv. Doz. Dr. Ekkehard Peik

Matrikelnummer: 10011066

Ausgabedatum: 31. August 2022
Abgabedatum: 12. Juni 2023

Eigenständigkeitserklärung

Hiermit versichere ich, die vorliegende Abschlussarbeit selbstständig und nur unter Verwendung der von mir angegebenen Quellen und Hilfsmittel verfasst zu haben. Sowohl inhaltlich als auch wörtlich entnommene Inhalte wurden als solche kenntlich gemacht. Die Arbeit hat in dieser oder vergleichbarer Form noch keinem anderem Prüfungsgremium vorgelegen.

Hannover, den 12.06.2023

Kai Christian Grensemann

Contents

CHAPTER 1

Introduction

Local Lorentz invariance (LLI) is one of the three fundamental symmetries of Einstein's equivalence principle [1]. Together with the universality of free fall and local position invariance, it builds the foundation for the general theory of relativity (GR) [2], one of the most successful modern theories in physics. GR fully describes the fundamental force of gravitation at macroscopic levels, however not satisfactory at the quantum level. Next to GR, the also highly successful theory called the standard model of particle physics (SM) describes all three remaining fundamental forces, the electromagnetic force, the weak and the strong force. One of the big governing questions in modern physics is whether a comprehensive theory of everything can be found, that unifies all four fundamental forces consistently. In an effort to accomplish this unification, it has been suggested that the violation of GR's fundamental symmetries, in particular Lorentz violation (LV), could take place at the quantum level [3, 4]. Therefore, experimental searches for LV are an important aspect in searches for new physics.

A wide range of experiments at different energy scales and in different particle sectors have been conducted in the past decades in search of LV, both on earth and via astrophysical observations [5]. Among them are modern Michelson-Morley analogues based on high-finesse optical cavities [6, 7] and the evaluation of measured high-energy cosmic background radiation [8, 9]. Recent advancements in high precision spectroscopy of trapped ions have made these systems an attractive platform for the search of low-energy LV in the combined electron-photon sector [10, 11, 12]. The current most accurate LLI test in that sector has been performed by Dreissen et al. [13], improving upper bounds for LV parameters to the 10^{-21} level. It used a scalable method [14] based on radio frequency (rf) spectroscopy and dynamical decoupling (DD) in the highly sensitive $^2F_{7/2}$-manifold of a single $^{172}Yb^+$-ion.

The goal of this thesis is the scaling of the LLI test by Dreissen et al. to a ten-ion Coulomb crystal to improve the sensitivity to LV by a factor of $\sqrt{10}$. To achieve this, firstly a highly robust DD sequence is identified with the help of numerical simulations. Secondly, the spatial field gradients in the trapping region are measured spectroscopically and the magnetic field gradient is minimized to an acceptable level. Finally, simultaneous efficient optical excitation of six ions to the $^2F_{7/2}$-manifold is shown within an eight ion Coulomb crystal, using a holographic phaseplate to create a flat line-shaped laser beam profile. By solving a few remaining technical limitations, the shaped laser profile could in the future be used for the simultaneous excitation of ten ions at the right axial confinement for a sensitive LLI test.

This thesis is organized as follows. In **Chapter 2**, the theoretical framework for the LLI

test is introduced and the Ramsey-type spectroscopy sequence is described. After establishing optimal measurement parameters, an estimation of the achievable sensitivity with a ten-ion crystal is performed. Finally, an overview of the experimental setup is given.

Chapter 3 contains the numerical study of different DD schemes, with the goal of finding the most robust scheme against experimental rf pulse errors. After an introduction of the numerical implementation and sequence modelling, an intuitive spin-echoed DD sequence and several quantum information inspired sequences are compared. This is done visually on the Bloch sphere and quantitatively in the form of stability diagrams. Finally, the numerical method is validated by comparing stability diagrams with corresponding spectroscopic measurements in the $^2S_{1/2}$ ground state.

In **Chapter 4**, a measurement of the magnetic field and the rf transition driving field homogeneity is performed. Simultaneous Rabi spectroscopy of six ions in a 125 µm long Coulomb crystal on the electric quadrupole transition is used to measure the B-field gradient. A reduction of the B-field gradient to an acceptable level of less than 0.03 µG/µm is achieved by applying a differential current between the two coils providing the quantization field. The rf field inhomogeneity is measured with simultaneous extended Rabi flops in the $^2S_{1/2}$ manifold. Causing a maximum π-pulse duration deviation of 0.7% over the crystal, it does not require any reduction.

Chapter 5 presents the experimental setup used for the efficient simultaneous excitation of ions in Coulomb crystals from the $^2S_{1/2}$ to the $^2F_{7/2}$ state. A characterization of the shaped flat line profile is first performed with a high resolution beam profiling camera. An approximately 80 µm long segment with intensity variations smaller than 2% and a section with high intensity variations, likely caused by technical limitations of the setup, are observed. The flat section of the beam profile is used to address an 80 µm long ion crystal, demonstrating efficient excitation to the $^2F_{7/2}$ state at the same transition frequency within ± 1 Hz in six out of eight ions.

Finally, **Chapter 6** draws a conclusion of the acquired results and gives an outlook onto further improvements to achieve the goal of a ten-ion LLI test.

CHAPTER 2

Measurement scheme and experimental setup

This chapter introduces the measurement method for the LLI test and the experimental setup. First, the theoretical framework is introduced, in which LV is quantified and different LLI tests are compared. Within this framework, the sensitivity of the Yb^+-ion is compared to other species. Then, the physical description of a trapped ion interacting with a resonant rf field is given and the Ramsey-type spectroscopy sequence for the LLI measurement is explained. After establishing optimal measurement parameters, an estimation of the achievable sensitivity with a ten-ion crystal is performed. Finally, the most important components of the experimental setup are reviewed, namely the linear rf Paul trap, the lasers and the coil for generation of the resonant rf field.

2.1 Framework for spectroscopic tests of LLI

Local Lorentz invariance (LLI) is a fundamental assumption of the general theory of relativity, stating that the outcome of an experiment does not depend on its angular orientation in space. Testing this assumption in a quantum system requires a framework to quantify Lorentz violating effects on atomic scales. As the standard model of particle physics excludes the possibility of LV, a theoretical framework called the standard model extension (SME) [15] was developed. In the SME, the Lorentz violating tensor $c_{\mu\nu}$ is added to the kinetic term of the SM Lagrangian. After years of spectroscopic LLI tests in the electron-photon sector, no evidence of LV has been found and thus the components of the $c_{\mu\nu}$ tensor are constrained to the achieved experimental resolution [10, 11, 12, 13]. Because tensorial components depend on the reference frame, results of different experiments are compared in a common frame, the Sun-Centered Celestial Equatorial Frame (SCCEF).

All spectroscopic tests of LLI follow the same fundamental principal. In an apparatus located on Earth's surface, the energy difference ΔE between two differently oriented, ideally orthogonal, atomic orbitals is monitored as Earth rotates around its axis with a frequency of ω_{E} in the SCCEF. This is schematically shown in Fig. 2.1 for the LLI test method of this thesis, where ΔE is the splitting of the Zeeman sublevels in the $^2\mathrm{F}_{7/2}$-manifold of the $^{172}\mathrm{Yb}^+$-ion. If LLI holds, ΔE should be equal for all orientations of the apparatus. However, a measured modulation of ΔE with a frequency of ω_{E} would indicate LV. The experiment can be understood as resembling the Michelson-Morley interferometer used to measure the isotropy of the speed of light [16]. Instead of the photon propagation along the different arms, the oriented momentum distributions of atomic orbitals are used and Earth's rotation replaces the rotating table.

Similarly to the Lorentz symmetry test using Earth's rotation around its axis, local position invariance could also be tested by monitoring ΔE as Earth orbits the sun with frequency ω_{O}. This would however require to perform the experiment for longer durations on the order of a year and is not the goal of this thesis.

To realize differently oriented atomic orbitals in the experiment, two distinct methods have been used. One method is the operation of two separate optical atomic clocks with differently oriented quantization magnetic fields. This was accomplished by the authors of ref. [12], who used two clocks operating on the $^2\mathrm{S}_{1/2}$ to $^2\mathrm{F}_{7/2}$ E3 transition in trapped $^{171}\mathrm{Yb}^+$-ions. The challenge of this method is the necessity to operate two clocks at high levels in fractional frequency uncertainty. The second method is the use of a superposition of two orthogonal orbitals within the same ion and measurement of the energy difference by means of a phase accumulation in a Ramsey-type experiment. The challenge in the latter method is the necessity to suppress magnetic field noise during the free evolution time. One way to achieve this is the use of entanglement to create decoherence free states [10]. Another way was proposed in ref. [14], based on dynamical decoupling with rf pulses. The latter was successfully used to test LLI in a single $^{172}\mathrm{Yb}^+$-ion in the same setup as used for this thesis, setting the current most stringent bounds of $c_{\mu\nu}$ tensor components in the electron-photon sector at the 10^{-21}-level [13]. This method only requires one experimental setup and most systematic frequency shifts are common mode to the differently oriented orbitals. In addition, it is readily scalable to multiple ions in a Coulomb crystal.

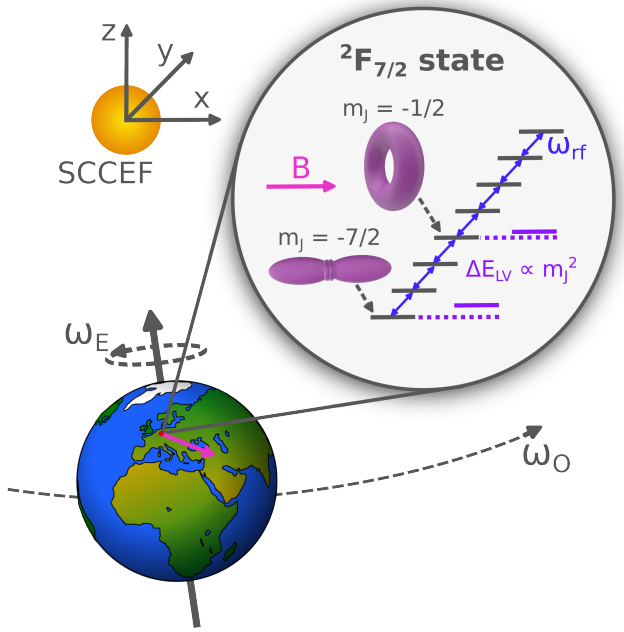

Figure 2.1: Schematic representation of the LLI test method of ref. [13] and this thesis. Within the $^2F_{7/2}$-manifold of the $^{172}Yb^+$-ion, the quadratic sublevel splitting is monitored, while the orientation of the quantization B-field rotates with Earth in the Sun Centered Celestial Equatorial Frame (SCCEF).

2.2 Yb^+ as a candidate for tests of LLI

The Yb^+ ion is an ideal system to test LLI. Its low lying $^2F_{7/2}$ state is highly sensitive to LV [14], has an extremely long radiative lifetime of 1.6 years [17] and can be coherently populated on an optical transition [18]. This section explains how the sensitivity to LV is extracted from the SME.

In the SME framework, LV causes small energy shifts to bound electronic states given by the Hamiltonian [19, 20]

$$\delta\mathcal{H} = -\left(C_0^{(0)} - \frac{2U}{3c^2}c_{00}\right)\frac{p^2}{2} - \frac{1}{6}C_0^{(2)}T_0^{(2)}. \tag{2.1}$$

$C_0^{(0)}$, c_{00} and $C_0^{(2)}$ contain components of the $c_{\mu\nu}$ tensor. The first term in Eq. 2.1 is constant for all substates $|J, m_J\rangle$ of an electronic state. However, the second term contains the $T_0^{(2)}$ operator, with the relativistic form $T_0^{(2)} = c\gamma_0(\gamma p - 3\gamma_z p_z)$, where γ_0 and γ are Dirac matrices. Its matrix element is given by [14]

$$\left\langle J, m_J \middle| T_0^{(2)} \middle| J, m_J \right\rangle = \frac{-J(J+1) + 3m_J^2}{\sqrt{(2J+3)(J+1)(2J+1)J(2J-1)}} \cdot \left\langle J \middle\| T^{(2)} \middle\| J \right\rangle, \tag{2.2}$$

where m_J is the projection of the total angular momentum J on the quantization axis. Thus, the matrix element contains a term proportional to the product of m_J^2 and the reduced matrix element $\langle J \| T^{(2)} \| J \rangle$, which results in a quadratic energy shift of the Zeeman sublevels of a given electronic state. This energy shift can be used to search for LV in the LLI test method of

this thesis. In the theoretical description of the physical system given in the next section, the quadratic shift will be considered in the form of the Hamiltonian

$$\mathcal{H}_{\mathrm{LV}}(t) = \kappa_{\mathrm{LV}}(t) J_z^2, \tag{2.3}$$

where $\kappa_{\mathrm{LV}}(t)$ is the quadratic energy shift magnitude.

The most precise test of LLI can be achieved with a system in which small $c_{\mu\nu}$ components cause large energy shifts. Equations 2.1 and 2.2 show that, for such a precise test, the difference $\Delta|m_J|$ between two states and the reduced matrix element should be as large as possible. In Table 2.1, the reduced matrix elements and LV energy shifts, normalized by $C_0^{(2)}$, are given for the most promising ionic and atomic species [14]. Yb^+ is an order of magnitude more sensitive to LV than the previously used Ca^+ [10], because both the reduced matrix element and the highest possible $\Delta|m_J|$ are larger. The LLI test method used for this thesis utilizes a superposition of all Zeeman substates in the $^2\mathrm{F}_{7/2}$ state and takes advantage of the highest possible $\Delta|m_J|$.

Future LLI tests could benefit from even higher sensitivities to LV provided by a variety of highly charged ions (HCIs). For example, U^{34+} has a state with a sensitivity of $|\Delta E/(hC_0^{(2)})| = 3.0 \times 10^{17}$ Hz [14]. However, the proposed HCI states are not spectroscopically accessible at present.

Ion/atom	Level	J	$\langle J\|\|T^{(2)}\|\|J\rangle$ (a.u.)	$\|\Delta E/(hC_0^{(2)})\|$ (Hz)
Ca^+	$3d$	5/2	9.3	4.5×10^{15}
Yb^+	$4f^{13}6s^2$	7/2	135	6.1×10^{16}
Tm	$4f^{13}6s^2$	7/2	141	6.4×10^{16}
Yb	$4f^{13}5d6s^2$	2	74	3.9×10^{16}

Table 2.1: Most sensitive singly charged ions and atoms to LV [14]. For each system the sensitive level with the respective total angular momentum J, the reduced matrix element of the $T^{(2)}$ operator and the normalized energy shift due to LV is given.

2.3 Measurement method using composite rf pulse spectroscopy

A big challenge in conducting the LLI test in $^{172}\mathrm{Yb}^+$ is the first order magnetic field sensitivity. Ambient magnetic field noise in the lab introduces orders of magnitudes larger energy shifts than LV might. In order to precisely measure the quadratic energy splitting of the Zeeman sublevels in the $^2\mathrm{F}_{7/2}$ state, while mitigating noise from the ambient magnetic field, a Ramsey-type spectroscopy sequence is used, where dynamical decoupling (DD) with radio frequency (rf) π-pulses is implemented during the free evolution time. This method was theoretically proposed by R. Shaniv et al. [14] and used for the single-ion LLI test by L.S. Dreissen et al. [13] with a more robust DD scheme.

In this section, the physical system of a Zeeman sensitive state, interacting with a resonant rf field is introduced. Building up on this, the Ramsey-type spectroscopy sequence is explained and optimal measurement parameters are shown to achieve the most sensitive LV measurement signal. The entire section closely follows the work of R. Shaniv et al. [14].

Physical system

First, a Zeeman sensitive state with a total angular momentum of J is considered. It interacts with an applied magnetic quantization field $\mathbf{B} = B_z\hat{\mathbf{z}}$ via its magnetic moment μ_z. The total free evolution Hamiltonian of this state is composed of a linear and a quadratic term according to

$$\mathcal{H}_{\text{free}} = \mathcal{H}_{\text{lin}} + \mathcal{H}_{\text{quad}}. \tag{2.4}$$

The linear part is given by

$$\mathcal{H}_{\text{lin}} = \mu_z B_z J_z, \tag{2.5}$$

where J_z is the z-component of the angular momentum operator. It describes the linear Zeeman shift of the energy eigenstates $|J, m_J\rangle$ due to the magnetic field. The quadratic part, given by

$$\mathcal{H}_{\text{quad}} = \kappa(t) J_z^2, \tag{2.6}$$

takes into account the electric quadrupole shift induced by the gradient of the trapping field and a potential Lorentz violating (LV) signal. The quadratic shift magnitude

$$\kappa(t) = \kappa_{\text{QS}} + \kappa_{\text{LV}}(t) \tag{2.7}$$

is composed of a constant contribution κ_{QS} from the electric quadrupole shift and a much smaller potential contribution $\kappa_{\text{LV}}(t)$ from LV, oscillating with Earth's rotation frequency and its harmonics. In the case of the $^2\text{S}_{1/2}$ ground state, $\kappa(t)$ is zero, because the atomic orbitals are spherical.

When an rf driving field with frequency ω_{rf} close to resonance $\omega_0 = \mu_z B_z/\hbar$ with the transition between neighboring, to first order equally spaced, Zeeman states is applied, the evolution of the system is given by the coupling Hamiltonian

$$\mathcal{H}_{\text{coup}} = \Omega(t)\, \cos(\omega_{rf} t + \phi)\, J_x \tag{2.8}$$

with the multi-level Rabi frequency Ω and the rf phase ϕ. As the magnetic field at the ion position, and thus the resonance $\omega_0(t)$, can drift over time, a time-dependent rf detuning $\delta(t)$ is considered such that $\omega_{rf} = \omega_0(t) + \delta(t)$. In total, and after applying the rotating wave approximation, the Hamiltonian has the form

$$\mathcal{H} = \delta(t) J_z + \kappa J_z^2 + \Omega(t)[J_x \cos(\phi) - J_y \sin(\phi)], \tag{2.9}$$

where J_x and J_y denote the x- and y-component of the total angular momentum operator respectively. During applied rf pulses, the Rabi frequency is assumed constant, $\Omega(t) = \Omega_0$, and much larger than δ and κ. Between rf pulses, $\Omega(t) = 0$ is assumed.

Ramsey-type spectroscopy sequence

The Ramsey-type spectroscopy method with DD is used to measure the quadratic level splitting strength κ, while mitigating magnetic field noise causing a detuning δ. Here, a specific DD scheme with an intuitive rephasing method is assumed, which is also used in the theoretical proposal [14]. Ch. 3 of this thesis contains a study of different DD schemes and concludes in the use of a more complex scheme that improves the robustness against experimental rf pulse errors.

At the beginning of the sequence, the ion is prepared in a specific Zeeman substate $|J, m_J\rangle$. In our experiment this is achieved by optically exciting the ion from the $\left|{}^2S_{1/2}, m_J = -1/2\right\rangle$ state to the $\left|{}^2F_{7/2}, m_J = -1/2\right\rangle$ state with a π-pulse on the electric octupole (E3) transition. The evolution of the state throughout the entire rf sequence is shown in Fig. 2.2. A resonant rf $\pi/2$-pulse of duration $t = \pi/(2\Omega)$ (1) is used to create a superposition between all substates in the J-manifold. Its phase is defined as $\phi = 0$. A first free evolution dark time of duration t_w follows, during which the detuning δ and κ cause a phase accumulation of the state along the equator of the Bloch sphere (2). As typically $\kappa \ll \delta$, only the phase due to δ is shown in Fig. 2.2. Next, a π-pulse with $\phi = \pi/2$ (3) is used to effectively translate the state backwards on the equator. Another free evolution dark time follows, with duration $2t_w$ (4). A second π-pulse with $\phi = -\pi/2$ (5) is used to again translate the state backwards on the equator, this time rotating the state across the opposite hemisphere. After a final free evolution time of t_w (6), a detection $\pi/2$-pulse with $\phi = \phi_d$ (7) projects the state onto the initial Zeeman substate. In Fig. 2.2, $\phi_d = \pi$ was chosen. Later in this section it is shown that this phase results in the highest measurement sensitivity. The retrieved population fraction $|\langle m_J|\Psi_{\text{final}}\rangle|^2$ indicates the total phase accumulated during the sequence. In our experiment it is measured by deexciting the ion back to the ground state with an E3 π-pulse and performing fluorescence detection on the ${}^2\mathrm{S}_{1/2}$ to ${}^2\mathrm{P}_{1/2}$ dipole transition.

It can be shown mathematically, that the phase accumulation due to the quadratic level splitting is coherently accumulated (not shown in Fig. 2.2), while the phase accumulation due to the linear Zeeman shift is compensated by the rephasing π-pulses. The total free evolution dark time T_D can be extended by repeating the single DD cycle between steps (2) and (6) n times.

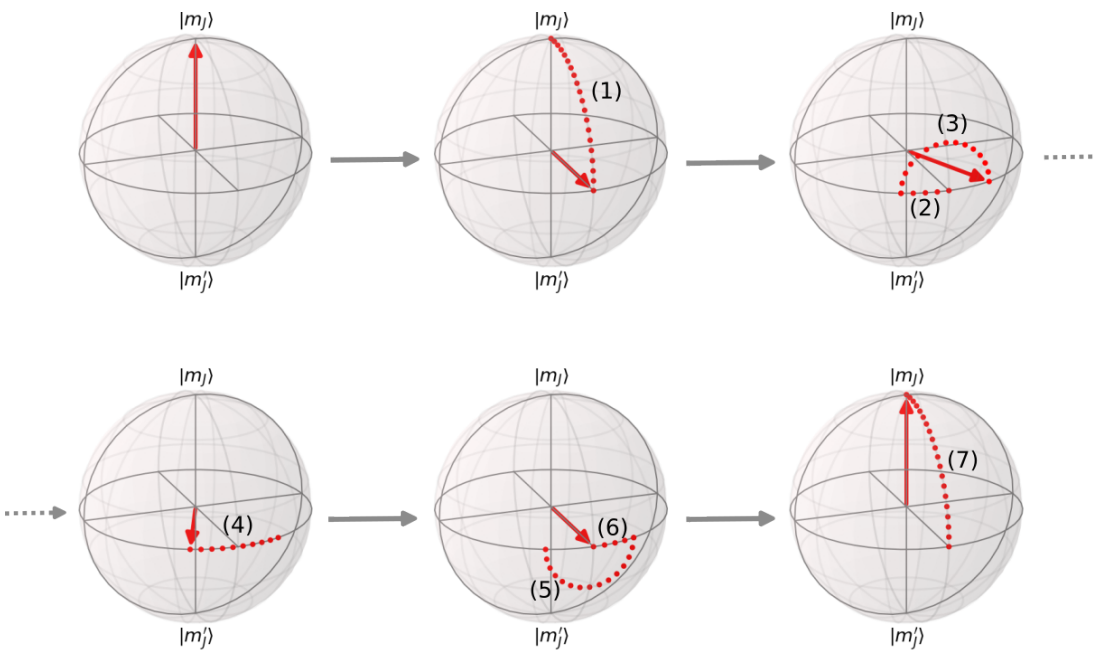

Figure 2.2: Generalized Bloch sphere representation of the Ramsey-type spectroscopy sequence with an intuitive spin-echoed DD scheme [14]. As the scheme is applied in the eight-level ${}^2\mathrm{F}_{7/2}$ manifold, the quantum mechanical state cannot be represented on a true Bloch sphere. An interpretation of the generalized Bloch sphere representation is given in Sec. 3.2.

Optimal measurement parameters

The experimentally tunable parameters for conducting the LLI test are the phase ϕ_d of the last $\pi/2$-pulse, the magnitude of κ_{QS} and the total dark time T_D after which the retrieved fractional population is monitored. All these parameters need to be chosen to minimize the measurement uncertainty $\Delta\kappa$. The total evolution of the state during the spectroscopy sequence, independent of the chosen DD scheme, is described by the operator

$$\mathcal{U}(\kappa T_D, \phi_d) = \exp\left(\frac{\pi}{2}\left(J_x \cos(\phi_d) - J_y \sin(\phi_d)\right)\right) \cdot \exp\left(i\kappa T_D J_z^2\right) \exp\left(\frac{\pi}{2} J_x\right), \tag{2.10}$$

which is derived in ref. [14]. For an initial state of $|m_J = -1/2\rangle$, the retrieved population fraction $P_{\mathrm{ret}}(\kappa T_D, \phi_d) = |\langle m_J|\mathcal{U}(\kappa T_D, \phi)|m_J\rangle|^2$ is plotted in Fig. 2.3 (a) for a range of ϕ_d and κT_D. The measurement outcome is 2π-periodic in ϕ_d and π-periodic in κT_D. The most sensitive measurement of κ is performed at the point in the plot, where $|dP_{\mathrm{ret}}/d\kappa|$ is largest. This point lies along the orange arrow in the figure, corresponding to $\phi_d = \pi$. At this fixed phase, Fig. 2.3 (b) shows the signal P_{ret} over κT_D. The highest slope is found at the point on the central fringe, where $P_{\mathrm{ret}} = 0.5$.

The magnitude of κ, with the dominant contribution κ_{QS} can be tuned by adjusting the axial confinement in the linear Paul trap, changing the electric field gradient and thus the electric quadrupole shift. To be sensitive to the smallest $\Delta\kappa_{\mathrm{LV}}$, κ_{QS} should be reduced to as small as possible, while the increased T_D stays within the experimentally achievable coherence time.

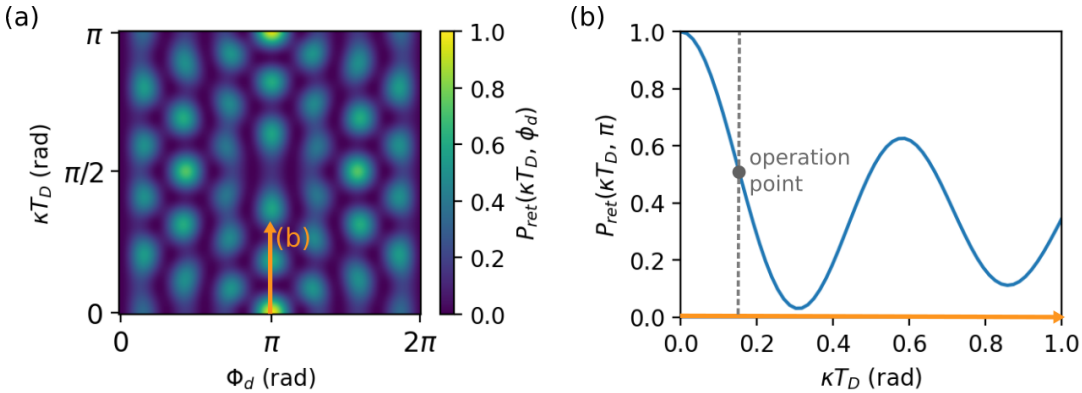

Figure 2.3: Retrieved population fraction P_{ret} at the end of the spectroscopy sequence for different measurement parameters. (a) shows P_{ret} for a variation of both κT_D and ϕ_d. (b) shows the Ramsey fringe at a fixed final pulse phase $\phi_d = \pi$, indication the operation point for the LLI test.

2.4 Sensitivity estimation for a multi-ion measurement

A potential LV signal would be measured as a modulation of $\kappa_{\mathrm{LV}}(t)$ with Earth's rotation frequency or its harmonics on top of the constant κ_{QS}. The inaccuracy of the measurement of κ is given as the standard deviation $\Delta\kappa$. It is related to the slope of the curve $P_{\mathrm{ret}}(\kappa T_D)$ and the quantum projection noise at the operation point. In this section, $\Delta\kappa$ is discussed for a measurement with a single ion and for the targeted measurement with 10 ions, considering the different quadrupole shifts along the crystal.

Single ion sensitivity

The following derivation follows ref. [14]. The outcome of the Ramsey experiment after n repetitions is $Y = \frac{1}{n}\sum_{i=1}^{n} x_i$ with $x_i \in \{0, 1\}$. The smallest measurable resolution $\Delta\kappa$ is then given by

$$\Delta\kappa = \left(\frac{dE[Y]}{d\kappa}\right)^{-1} \sqrt{V[E[Y]]} \tag{2.11}$$

with the expectation value $E[Y]$ and variance $V[E[Y]]$. The expectation value of Y is the population retrieval probability $P_{\mathrm{ret}}(\chi_{\mathrm{op}})$ at the operation point $\chi_{\mathrm{op}} = \kappa T_D$. The variance is assumed to be given by quantum projection noise. In total, this leads to

$$\Delta\kappa(\chi_{\mathrm{op}}) = \frac{\sqrt{P_{\mathrm{ret}}(\chi_{\mathrm{op}})\,(1 - P_{\mathrm{ret}}(\chi_{\mathrm{op}}))}}{\sqrt{\tau T_D} \cdot \frac{d}{d\chi} P_{\mathrm{ret}}(\chi)\Big|_{\chi=\chi_{op}}}, \tag{2.12}$$

where $\tau = nT_D$ is the total measurement time. For the case of the Yb^+-ion, an initial state of $|m_J = -1/2\rangle$, an optimal final rf phase $\phi_d = \pi$ and the optimal operation point $\chi_{\mathrm{op}} = 0.15\,\mathrm{rad}$, Eq. 2.12 can be simplified to $\Delta\kappa = 0.1\,(\mathrm{rad}/\sqrt{\tau T_D})$.

Sensitivity of a ten ion crystal

Conceptually, it is equivalent to perform the Ramsey experiment ten times with a single ion and once with ten uncorrelated ions. Therefore, ref. [14] gives the sensitivity $\Delta\kappa = 0.1(\mathrm{rad}/\sqrt{N\tau T_D})$ for a measurement with N Yb^+-ions at optimal parameters. However, the simple $\sqrt{N}$-scaling neglects that ions in a linear crystal are exposed to different electric field gradients, leading to different quadrupole shifts. As a result, the ions do not contribute identically to the measurement sensitivity. In the following, the reduced sensitivity due to this effect is calculated for a ten ion crystal at the same axial secular frequency of $\nu_{\mathrm{ax}} = 266\,\mathrm{kHz}$ as used for the single ion LLI test [13].

For each ion i in the crystal, the individual κ_i at $\nu_{\mathrm{ax}} = 266\,\mathrm{kHz}$ is calculated in Appendix A.1, taking into account the electric field gradients from the trapping field and the other ions. The results are

$$(\kappa_i) = (0.148,\ 0.174,\ 0.194,\ 0.207,\ 0.214,\ 0.214,\ 0.207,\ 0.194,\ 0.174,\ 0.148)\,\mathrm{rad\,Hz}, \tag{2.13}$$

where $\kappa = 0.13\,\mathrm{rad\,Hz}$ was measured for the single ion LLI test. The resulting measurement signal $P_{\mathrm{ret,i}}(T_D)$ for all ions is shown in Fig. 2.4 (a) according to Eq. 2.10. It is apparent that the highest slope $dP_{\mathrm{ret,i}}/d\kappa$ occurs at different dark times for outer and inner ions of the crystal. The total measurement sensitivity is obtained by using Eq. 2.11 and taking the sum of all $P_{\mathrm{ret,i}}(T_D)$ as the expectation value E, as well as the sum of all quantum projection noises for the variance V. This results in

$$\Delta\kappa(T_D) = \frac{\sqrt{\sum_{i=1}^{N} P_{\mathrm{ret,i}}(T_D)\,(1 - P_{\mathrm{ret,i}}(T_D))}}{\sqrt{\frac{\tau}{T_D}} \cdot \frac{d}{d\kappa}\sum_{i=1}^{N} P_{\mathrm{ret,i}}(T_D)}. \tag{2.14}$$

Using the κ_i from Eq. 2.13, the total sensitivity $\Delta\kappa(T_D)$ is displayed in Fig. 2.4 (b) as the solid blue line. In comparison, the simple $\sqrt{N}$-scaling for ten ions is displayed as a black dashed line and the sensitivity for a measurement with a single ion as a grey dotted line. At the optimal

dark time of $T_D = 1.13\,\mathrm{s}$ a sensitivity of $\Delta\kappa = 0.045\,\mathrm{rad}\sqrt{\mathrm{Hz}}/\sqrt{\tau}$ is achieved. This is a factor of 2.2 times more sensitive than the single ion measurement at $T_D = 1.13\,\mathrm{s}$, instead of $\sqrt{10} \approx 3.16$ times more sensitive. It should be noted that the factor of 2.2 only applies to a measurement at $\nu_{\mathrm{ax}} = 266\,\mathrm{kHz}$. At higher axial secular frequencies, and thus closer ion spacing, the improvement factor in respect to a single ion measurement decreases, because the electric field gradient varies more from ion to ion.

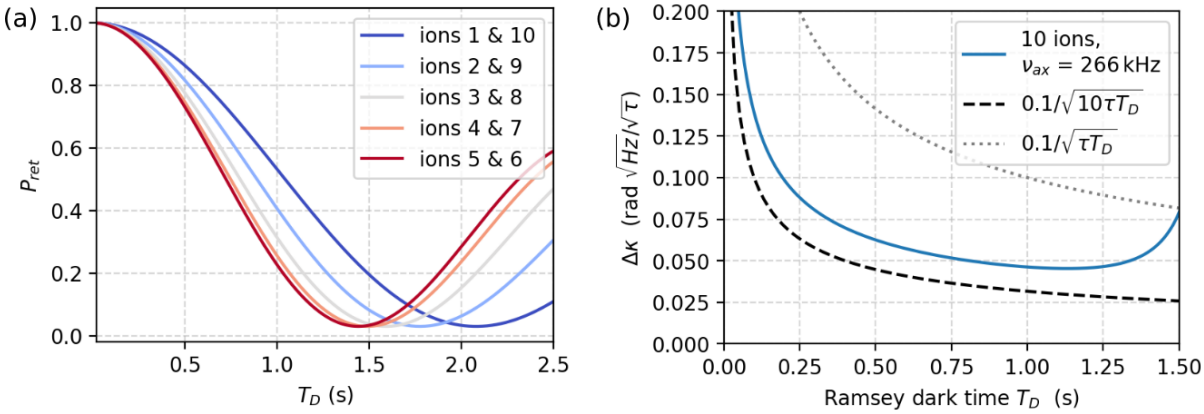

Figure 2.4: Sensitivity $\Delta\kappa$ of an LLI test using a ten ion crystal and an axial secular frequency of $\nu_{\mathrm{ax}} = 266\,\mathrm{kHz}$. (a) Shows the calculated retrieved population fractions for the different ions. The calculation of the used quadrupole shifts can be found in Appendix A.1. (b) shows $\Delta\kappa$ as given in Eq. 2.14 for a varied dark time as a solid blue line. For comparison, the sensitivity of a single ion measurement and a $\sqrt{10}$-improvement are shown as a dotted grey and dashed black line respectively.

2.5 Experimental setup

In the following, the setup for the experimental work of this thesis is described. The most important components of this setup include the ion trap, the lasers used for driving optical transitions and the coil that supplies the resonant rf field to drive transitions between Zeeman sublevels. All of these components have been built up and characterized prior to this thesis. The adjustments made during the work of this thesis are discussed in chapters 4 and 5.

Ion trap

The ions are trapped in a segmented linear rf-Paul trap. Detailed information about the design and characterization of the trap can be found in Refs. [21, 22]. The radial confinement is achieved with an rf quadrupole field supplied by a resonant circuit with a frequency of 24.38 MHz. In the axial direction eight segments are separated by DC electrodes, of which seven have a length of 1 mm and one a length of 2 mm. In continuation of preexisting beam alignment, the long segment was used for all experiments performed in this work.

Yb^+-ions are loaded into the trap by optical ablation of an Yb target and a subsequent isotope selective photo-ionization. The target contains a natural abundance of Yb, allowing to trap all stable isotopes in the setup. For historic reasons, the ^{172}Yb isotope was used for all experiments of this thesis.

Lasers

For the preparation, coherent manipulation and readout of electronic states, a range of optical transitions need to be addressed. Fig. 2.5 shows a reduced level scheme of the $^{172}Yb^+$ ion with the available laser driven transitions represented by the solid colored lines and natural decay channels by dashed gray lines.

The dipole allowed transition from $^2S_{1/2}$ to $^2P_{1/2}$ is driven with a frequency-doubled diode laser near 370 nm. It is used for Doppler cooling of the ions, florescence detection and optical pumping to a desired Zeeman sublevel of the ground state. The light is delivered to the ions from three different directions H1, H2 and V so that all motional modes can be cooled efficiently. For optical pumping into either of the $m_J = \pm 1/2$ sublevels, $\sigma^{\pm}$-polarized light is applied in the H2 direction in parallel to the orientation of the quantization magnetic field. As the ions can decay from the excited $^2P_{1/2}$ state to the metastable $^2D_{3/2}$ state, a repumper laser near 935nm is used to close the transition cycle.

The electric quadrupole (E2) transition from $^2S_{1/2}$ to $^2D_{5/2}$ near 411 nm is used in this thesis to accurately measure the magnetic field gradient along ion Coulomb crystals. It is driven by a frequency-doubled diode laser, stabilized to a ULE cavity [23]. Optionally, the laser can be locked to a Silicon cavity in Paschen-Bau via a transfer lock. Repumper lasers near 1650 nm, 636 nm and 935 nm are used to transfer the population back to the ground state after 411 nm light is applied in a sequence.

Finally, the highly forbidden electric octupole (E3) transition from $^2S_{1/2}$ to $^2F_{7/2}$ near 467 nm is used to efficiently populate and depopulate the $^2F_{7/2}$ state at the beginning and end of the LLI test sequence. This transition is extremely narrow with a natural linewidth in the nHz range and difficult to coherently address in a Zeeman sensitive even isotope. For a coherent manipulation on this transition, suppressed ambient magnetic field noise and a narrow, highly stable laser are required [18]. In the setup, an active magnetic field stabilization is implemented in the form of a feedback loop [24] supplying a signal from a magnetic field sensor near the trapping region to three pairs of magnetic field coils oriented in orthogonal directions. The transition driving laser is derived from the fundamental 934 nm laser of the single $^{171}Yb^+$-ion clock [25] operated by department 4.4 at PTB. A light fraction of the laser locked to the E3 transition of the clock ion is sent from Kopfermann-Bau to Giebe-Bau via a telecommunication fiber. It is first amplified with a laser diode, then the isotope shift close to 4.7 GHz is bridged with a high frequency AOM. Details on this setup can be found in Ref. [26].

After bridging the isotope shift, two separate light paths for single and multi ion addressing are available. The original single ion addressing path uses a second laser diode amplification stage and waveguide second harmonic generation (SHG) to achieve $\approx$ 12 mW of 467 nm light focused to a Gaussian spot with dimensions $w_x = 26\,\mu m$ and $w_y = 38$ nm at the ion. An intensity stabilization is implemented with an AOM operating at 200 MHz and frequency scanning with a double-pass 110 MHz AOM, both supplied by a direct digital synthesizer (DDS) [18, 26].

The newer multi-ion addressing path uses a commercial system[1] of fiber coupled tapered amplifier and SHG cavity. During the experimental work of this thesis a maximum 467 nm power of 210 mW was measured after the output fiber of the SHG cavity. A copy of the single ion addressing intensity stabilization and frequency scanning setup was built up during this work. At the end of this setup a maximum power of 91 mW was observed. After the transmission through a mode-cleaning optical fiber and a beam shaping holographic phaseplate, a final power of 36 mW entering the experimental chamber was achieved.

[1] supplied by Toptica

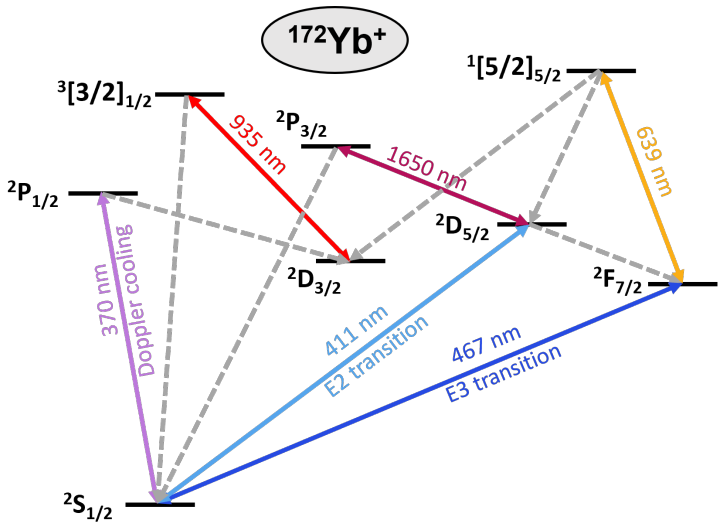

Figure 2.5: Energy level diagram of the $^{172}Yb^{+}$ ion [27]. The available laser transitions are marked as solid colored lines and natural decay channels as gray dashed lines.

Transition driving rf field

The rf field is supplied by a coil placed outside of the vacuum chamber. It consists of 27 turns wound at a diameter of 4.5 cm and has a distance of 5.5 cm to the ions. The coil has a measured resonance frequency of $\omega_{\mathrm{rf}}/2\pi = 3.5147\,\mathrm{MHz}$ [26] and is powered by a DDS referenced to a hydrogen maser. By adjusting the strength of the quantization magnetic field, the Zeeman splitting in the $^2\mathrm{S}_{1/2}$ or the $^2\mathrm{F}_{7/2}$ state can be brought close to resonance with ω_{rf}. A fine adjustment of ω_{rf} is then performed by tuning the DDS frequency to achieve the resonance. In the $^2\mathrm{F}_{7/2}$ state a multi-level Rabi frequency of roughly $\Omega = 33\,\mathrm{kHz}$ is achieved.

CHAPTER 3

Improvement of dynamical decoupling

This chapter presents the numerical and experimental study of different dynamical decoupling (DD) rf pulse sequences, with the goal of finding a highly robust sequence against experimental pulse imperfections. The experiment especially suffers from ambient magnetic field drifts, which induce a detuning δ between the fixed rf driving frequency and the drifting atomic resonance, and from drifts in the rf power provided by the macroscopic coil, which cause pulse duration errors Δt. The proposed spin-echoed DD sequence [28] lead to a limited coherence time on the order of a few milli seconds during the Ramsey dark time of our LLI test. Only after an implementation of the highly robust UR10 sequence [29], the coherence time was extended to seconds [13], enabling a sensitive LLI test.

In the beginning of this chapter, the numerical implementation of the physical system of Sec. 2.3 is introduced. It is used to show the more complex dynamics of coherent manipulation in an eight-level system compared to the well known dynamics in a two-level system, making operations in the eight-level system more susceptible to fidelity loss from rf pulse imperfections.

After an introduction to the numeric modelling method for entire composite pulse sequences, the DD schemes under test are introduced and visualized on the generalized Bloch sphere. Following that, the robustness against the rf pulse induced errors δ and Δt is evaluated quantitatively in the form of stability diagrams.

Finally, the numerical methods are validated experimentally with a comparison of simulated stability diagrams to measurements in the $^2S_{1/2}$ manifold.

3.1 Numerical model

In order to numerically study the composite pulse sequences for dynamical decoupling (DD), the atomic system and its interaction with the applied radio frequency (rf) field is described in the full quantum picture, using the Hamiltonian given in Eq. 2.9. This description allows to simulate the rf sequence in the $^{172}\mathrm{Yb}^{+}$-ion's $^{2}\mathrm{F}_{7/2}$ state for a test of LLI, as well as in the $^{2}\mathrm{S}_{1/2}$ ground state for experimental verification of the simulation. Here, the explicit numerical implementation of the used operators and the calculation of the time evolution are shown.

Numerical implementation

All calculations and simulations presented in this chapter are performed in Python. The quantum mechanical state in a J-manifold is represented by an array

$$\Psi = (\alpha_{-J},\, \alpha_{-J+1},\, ...,\, \alpha_J), \tag{3.1}$$

containing the complex amplitudes of the energy eigenstates

$$\alpha_{m_J} = \langle J, m_J | \Psi \rangle \,. \tag{3.2}$$

In this basis, the matrix representation of the spin operators J_x, J_y and J_z takes the form of the well known Pauli spin matrices for the two-level system of the $^{2}\mathrm{S}_{1/2}$ ground state. In the eight-level system these operators are represented by the following 8×8-matrices

$$J_x = \begin{pmatrix} 0 & \frac{\sqrt{7}}{2} & 0 & 0 & 0 & 0 & 0 & 0 \\ \frac{\sqrt{7}}{2} & 0 & \sqrt{3} & 0 & 0 & 0 & 0 & 0 \\ 0 & \sqrt{3} & 0 & \frac{\sqrt{15}}{2} & 0 & 0 & 0 & 0 \\ 0 & 0 & \frac{\sqrt{15}}{2} & 0 & 2 & 0 & 0 & 0 \\ 0 & 0 & 0 & 2 & 0 & \frac{\sqrt{15}}{2} & 0 & 0 \\ 0 & 0 & 0 & 0 & \frac{\sqrt{15}}{2} & 0 & \sqrt{3} & 0 \\ 0 & 0 & 0 & 0 & 0 & \sqrt{3} & 0 & \frac{\sqrt{7}}{2} \\ 0 & 0 & 0 & 0 & 0 & 0 & \frac{\sqrt{7}}{2} & 0 \end{pmatrix} \tag{3.3a}$$

$$J_y = \begin{pmatrix} 0 & -\frac{i\sqrt{7}}{2} & 0 & 0 & 0 & 0 & 0 & 0 \\ \frac{i\sqrt{7}}{2} & 0 & -i\sqrt{3} & 0 & 0 & 0 & 0 & 0 \\ 0 & i\sqrt{3} & 0 & -\frac{i\sqrt{15}}{2} & 0 & 0 & 0 & 0 \\ 0 & 0 & \frac{i\sqrt{15}}{2} & 0 & -2i & 0 & 0 & 0 \\ 0 & 0 & 0 & 2i & 0 & -\frac{i\sqrt{15}}{2} & 0 & 0 \\ 0 & 0 & 0 & 0 & \frac{i\sqrt{15}}{2} & 0 & -i\sqrt{3} & 0 \\ 0 & 0 & 0 & 0 & 0 & i\sqrt{3} & 0 & -\frac{i\sqrt{7}}{2} \\ 0 & 0 & 0 & 0 & 0 & 0 & \frac{i\sqrt{7}}{2} & 0 \end{pmatrix} \tag{3.3b}$$

$$J_z = \begin{pmatrix} \frac{7}{2} & 0 & 0 & 0 & 0 & 0 & 0 & 0 \\ 0 & \frac{5}{2} & 0 & 0 & 0 & 0 & 0 & 0 \\ 0 & 0 & \frac{3}{2} & 0 & 0 & 0 & 0 & 0 \\ 0 & 0 & 0 & \frac{1}{2} & 0 & 0 & 0 & 0 \\ 0 & 0 & 0 & 0 & -\frac{1}{2} & 0 & 0 & 0 \\ 0 & 0 & 0 & 0 & 0 & -\frac{3}{2} & 0 & 0 \\ 0 & 0 & 0 & 0 & 0 & 0 & -\frac{5}{2} & 0 \\ 0 & 0 & 0 & 0 & 0 & 0 & 0 & -\frac{7}{2} \end{pmatrix}. \tag{3.3c}$$

The derivation of these matrices can be found in Appendix A.2. Using the spin matrices, Eq. 2.9 can be used to calculate the total Hamiltonian in matrix form.

Time dynamics

For the modeling of composite rf pulse sequences it is assumed that the total Hamiltonian is constant for the duration of a single rf pulse or free evolution time of 100 µs. The evolution of an initial state $|\Psi(t_0)\rangle$, subjected to a constant Hamiltonian $\mathcal{H}(t_0)$ for a duration of t, is given by

$$|\Psi(t_0+t)\rangle = \mathcal{U}(t_0,t)\ |\Psi(t_0)\rangle = \exp(-i\hbar t\,\mathcal{H}(t_0))\ |\Psi(t_0)\rangle\,. \tag{3.4}$$

Consequently, the entire evolution of the atomic state during an experiment can be calculated by applying a series of evolution operators $\mathcal{U}$, each containing fixed values of δ, κ, Ω and ϕ for the respective Hamiltonian. The necessary operator exponential

$$\exp(X) = \sum_{i=0}^{\infty} \frac{1}{k!} X^k \tag{3.5}$$

for an n×n-matrix X is computed using the *linalg.expm* method provided by the Python module *SciPy*, which uses the approximation algorithm presented in Ref. [30].

3.2 Dynamics of the $^2F_{7/2}$-manifold eight-level system

Using the introduced numerical implementation, the dynamics of the Zeeman substates in the eight-level $^2F_{7/2}$-manifold interacting with the rf field are simulated. They show key differences to the dynamics of a two-level system, in particular narrower spectral resonance features and narrower features in the time evolution. These properties reduce the allowed error margin for rf pulses in respect to rf detuning and pulse duration.

Simulated rf spectrum

Figure 3.1 compares the simulated spectra of a two-level system in (a) and an eight-level system in (b). Both spectra are calculated by assuming an initial state of $|m_J = -1/2\rangle$ and applying an evolution operator $\mathcal{U}(t = t_\pi)$ corresponding to an rf π-pulse of duration $t_\pi = \pi/\Omega$. The population of each substate $|\langle m_J|\Psi\rangle|^2$ after the interaction is shown for a varied rf detuning δ.

The result for the two-level system in (a) shows the central resonance feature of the well known Rabi spectrum. In the case of the eight-level system in (b) the central resonance is much more narrow in respect to Ω. Whereas a small detuning of $\delta/\Omega = 0.3$ only reduces the final population of the $|m_J = 1/2\rangle$ to $\approx 90\%$ for the two-level system, the same detuning causes a population reduction to zero in the eight-level system.

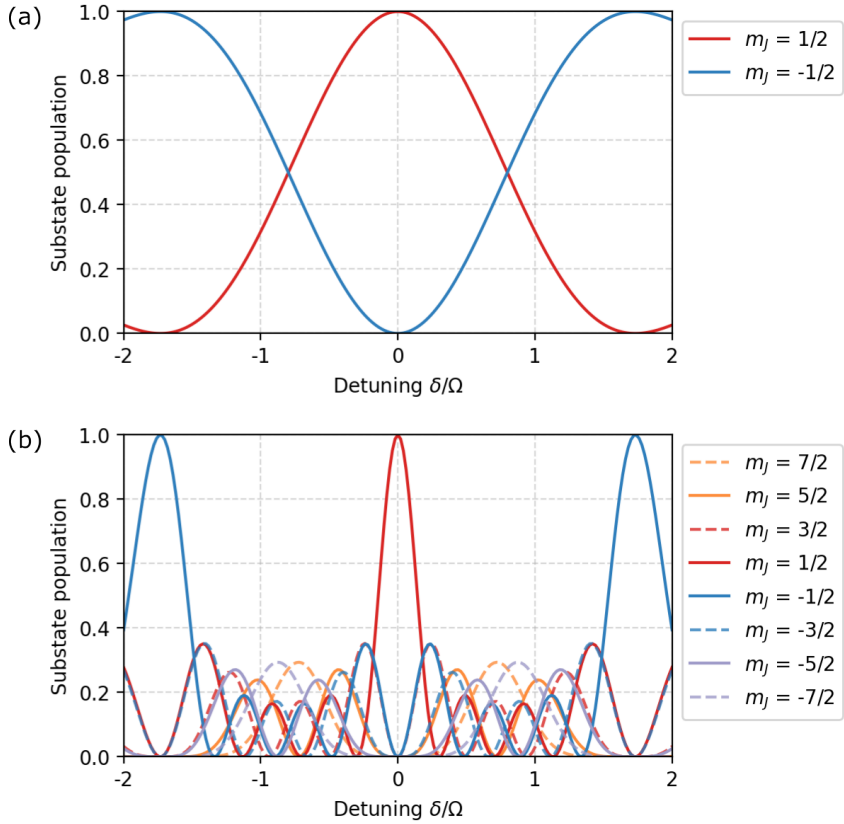

Figure 3.1: Simulated rf spectra for a two-level system (a) and an eight-level system (b), displaying the narrower resonance feature of the latter. For both spectra an initial state of $|m_J = -1/2\rangle$ and a pulse duration of $t_\pi = \pi/\Omega$ are assumed. The final population of each state is shown for a varied rf detuning δ.

Simulated time evolution

Figure 3.2 shows the time evolution of a two-level system in (a) and an eight-level system in (b) during the interaction with a resonant rf field ($\delta = 0$). For both systems, the initial state is again assumed to be $|m_J = -1/2\rangle$ and the final population of all states is shown for a varied interaction time t scaled to the π-pulse duration $t_\pi = \pi/\Omega$. The two-level system exhibits the well known sine-shaped population transfer between the two states, known as Rabi flops. The eight-level system, on the other hand, shows a more complex time evolution as the population spreads over all states of the manifold before it interferes constructively in the $|m_J = 1/2\rangle$ state after the π-pulse duration. Again, the time evolution feature corresponding to a high final population of the $|m_J = 1/2\rangle$ state around $t = t_\pi$ is much narrower than in the two-level case.

For two-level systems, the Bloch sphere is often used to visually represent the time evolution of the full quantum mechanical state during a composite pulse spectroscopy sequence. Although in general the Bloch sphere can only display enough degrees of freedom for a state in a two level system, it is used as a visualization tool for pulse sequences in the eight-level $^2\mathrm{F}_{7/2}$ manifold throughout this thesis. This choice is motivated by the overall similar time evolution of both systems, when the eight-level system is initially prepared in one of the $|m_J = \pm 1/2\rangle$ states. The two poles of the "generalized" Bloch sphere are the $|m_J = \pm 1/2\rangle$ substates and a $\pi/2$-pulse transfers the state from a pole the equator, where the state is in a superposition of all levels. The highly LV-sensitive levels $|m_J = \pm 7/2\rangle$ have the largest amplitude in equator states,

making them ideal probe states during the dark evolution time of the Ramsey-type spectroscopy sequence for the LLI test.

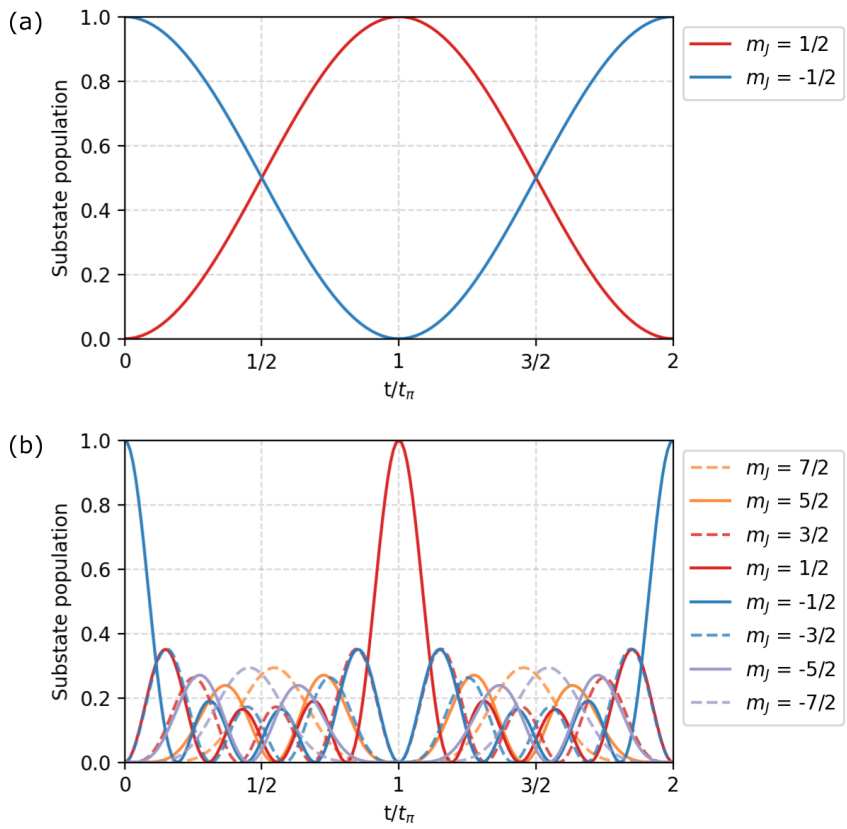

Figure 3.2: Simulated time evolution of a two-level system (a) and an eight-level system interacting with a resonant rf field ($\delta = 0$). For both systems an initial state of $|m_J = -1/2\rangle$ is assumed and the final population of all levels is shown after a varied interaction time t scaled to the π-pulse duration $t_\pi = \pi/\Omega$.

3.3 Modelling Ramsey-type experiments with dynamical decoupling

For modelling of the Ramsey-type experiment used to test LLI, a series of rf pulses and free evolution dark-times are applied. All rf sequences investigated in this chapter follow the same basic structure, ordering and labelling of pulses.

Figure 3.3 shows a schematic of the order in which the rf pulses and dark times are applied to the ion. The sequence always begins with a $\pi/2$-pulse with phase $\phi = 0$ to create a coherent superposition of Zeeman states within the corresponding J-manifold. After the initial pulse, the state evolves freely for the duration of the Ramsey dark time T_D until the final $\pi/2$-detection pulse with $\phi = \pi$ is applied to measure the phase that has accumulated. The evolution operators for these two pulses are denoted as $\mathcal{U}_{\pi/2,0}$ and $\mathcal{U}_{\pi/2,\pi}$ respectively, where the first index corresponds to the pulse duration and the second index to the phase.

During the Ramsey dark time, dynamical decoupling (DD) schemes are used to counteract the dephasing caused by the linear Zeeman shift, while maintaining the phase accumulated due to the quadratic shifts. Several different DD methods are studied in this thesis. All these are composite pulse schemes, where a single modulation sequence consists of n rephasing π-pulses

with different phases ϕ_i, that are separated by dark times of duration $2t_w$. The π-pulse evolution operators are denoted as $\mathcal{U}_{\pi,\phi_i}$ and t_w-duration dark time operators as $\mathcal{U}_{t_w}$. A single modulation sequence of a specific scheme is repeated N_{rep}-times, until the desired total dark time is reached as the sum of the individual dark times. In total, the final state $|\Psi_{final}\rangle$ is calculated as

$$|\Psi_{\text{final}}\rangle = \mathcal{U}_{\pi/2,\pi} \prod_{j=N_{\text{rep}}}^{1} \prod_{i=n}^{1} (\mathcal{U}_{t_w} \mathcal{U}_{\pi,\phi_i} \mathcal{U}_{t_w})_j \, \mathcal{U}_{\pi/2,0} \, |\Psi_0\rangle \,, \tag{3.6}$$

for a composite DD scheme with phases $(\phi_1, ..., \phi_n)$. As the operators have to be applied from the left, the indices of the products run in reverse from N_{rep}/n to 1. The total Ramsey dark time for this experiment is

$$T_D = N_{rep} \cdot n \cdot 2t_w. \tag{3.7}$$

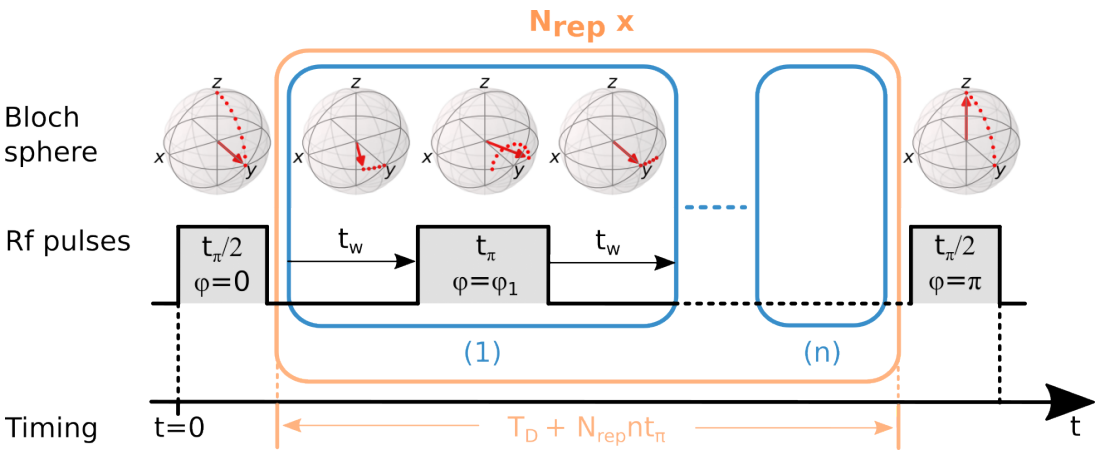

Figure 3.3: Schematic of Ramsey-type experiments with a composite pulse scheme for dynamical decoupling. The top row shows a Bloch sphere representation with a single exemplary rephasing pulse. The middle row shows rf-pulses of length $t_\pi/2$ or t_π and with phases ϕ relative to the initial pulse as shaded rectangles.

Fidelity of a composite pulse sequence

So far, the order, timing and phases of the rf pulses were discussed for an ideal case. In addition to that, the modelling method can also be used to simulate experimental imperfections, such as rf detunings or pulse duration errors. For the case of a constant detuning, the Hamiltonians used to calculate all evolution operators have to be constructed with $\delta \neq 0$. Similarly, constant pulse duration errors can be simulated by changing the duration of all π-pulses to $t = \pi/\Omega + \Delta t$. By introducing these types of pulse errors in the simulation of the experiment, the robustness of the experimental outcome against pulse imperfections can be characterized.

To quantify the robustness, the quantum mechanical fidelity ($\mathcal{F}$) is used. The fidelity of an experimental outcome $|\Psi_{\text{final}}\rangle$ is, essentially, the squared overlap with an ideal outcome $|\langle\Psi_{\text{ideal}}|\Psi_{\text{final}}\rangle|^2$. In the case of the presented Ramsey experiment the ideal outcome would be reached, if $\delta = 0$ and $\Delta t = 0$ throughout the duration of the full rf sequence. Therefore, the fidelity of a pulse sequence with a constant detuning δ and a constant pulse duration error for all π-pulses can be written as

$$\mathcal{F}(\delta,\, \Delta t) = |\langle\Psi_0|\mathcal{U}^\dagger_{\text{total}}(0,\, 0)\,\mathcal{U}_{\text{total}}(\delta,\, \Delta t)\,|\Psi_0\rangle|^2, \tag{3.8}$$

where $\mathcal{U}_{\text{total}}(\delta, \Delta t)$ is the product of all operators in Eq. 3.6.

3.4 Introduction of the studied sequences

In this thesis, a selection of four DD sequences is studied to find the best candidate for the LLI experiment. The first scheme is a generalized spin-echo sequence (GSE) for large spins, proposed by R. Shaniv et al. for the LLI test [14]. The spin-echo sequence has its origin in nuclear magnetic resonance [31] and has since also been successfully applied to precision spectroscopy of atomic transitions [28]. It consists of two π-pulses with phases given in Table 3.1. In the next section, its rephasing method will be explained intuitively on the Bloch sphere. Unfortunately, the GSE method fails when the rf-pulses contain detunings and pulse duration errors simultaneously, especially in the eight-level $^2F_{7/2}$-manifold with its narrow resonance features.

A more robust composite pulse method was introduced by G. Genov et al. in the context of quantum information processing [29], named universally robust (URX) sequences. These sequences with even numbers of pulses X contain theoretically optimized phases to compensate arbitrary pulse imperfections of increasing order with an increasing number of pulses. Here, the UR4, UR10 and UR16 sequences, with phases given in Table 3.1, are studied. The UR4 sequence will be compared to the similar GSE sequence to demonstrate the UR advantage. Following that, the UR10 and UR16 sequences will be studied numerically under aspects of robustness and suitability for the LLI test. The UR10 sequence was successfully used for the published single-ion LLI test [13], while the UR16 sequence is studied to quantify a potential robustness improvement for the planned multi-ion LLI test.

Sequence name	Rf phases ϕ_i in one DD cycle	Reference
Generalized spin echo (GSE)	(1, -1) $\pi/2$	[14]
UR4	(0, 1, 1, 0) π	[29]
UR10	(0, 4, 2, 4, 0, 0, 4, 2, 4, 0) $\pi/5$	[29]
UR16	(0, 1, 3, 6, 2, 7, 5, 4, 4, 5, 7, 2, 6, 3, 1, 0) $\pi/4$	[29]

Table 3.1: Phases of rf π-pulses for dynamical decoupling sequences studied in this thesis. It is to be noted that, although the same five phases are repeated twice in the UR10 sequence, only an application of all ten pulses yields a high fidelity.

GSE and UR4 schemes on the Bloch sphere

In this section, the state evolution during each of the studied sequences is shown in a Bloch sphere representation. The rephasing mechanisms are shown and, in the case of the GSE sequence, the strong fidelity loss with rf pulse errors is demonstrated intuitively. All Bloch sphere representations in this section were calculated with the numerical model introduced in the beginning of the chapter, applied to a two-level system. A Rabi frequency of $\Omega/2\pi = 33\,\text{kHz}$ and dark time of $t_w = 100\,\mu\text{s}$ were assumed as realistic lab values. To obtain sub-pulse-duration resolution, the evolution operators in Eq. 3.4 were computed for short durations of $t_\pi/30$ and $t_w/12$ for rf-pulses and dark times respectively. The states were plotted on the Bloch sphere using the *QuTiP*-package for Python.

The GSE sequence is composed of two π-pulses that rephase atomic states as they drift along the equator, due to linear energy shifts. Fig. 3.4 (a) shows a representation of this mechanism. An initial 50/50-superposition of ground and excited state with a fixed phase (1) drifts along the equator of the sphere due to an assumed detuning of $\delta/\Omega = 3\%$ throughout the sequence (2).

With the two π-pulses (3) and (5), the state is effectively translated backwards on the equator of the sphere via a rotation around the x-axis, so that the detuning-induced drift during the following dark-times rephases the state back into its initial condition (4) and (6). In summary, the mechanism works well as long as the detuning changes slowly compared to the duration of the sequence and the π-pulse duration errors are close to zero.

An example for the effect of significantly large pulse errors on the fidelity of the GSE sequence is given in Fig. 3.4 (b). While the same detuning of $\delta/\Omega = 3\%$ is assumed, the two pulses are now slightly too short ($\Delta t/t_\pi = -3\%$). As a result, the state drifts away from the equator and towards the poles of the sphere. A successive application of only a few cycles of the GSE sequence would completely destroy the fidelity of a Ramsey experiment. This makes the GSE sequence unfeasible for the LLI test, where thousands of pulses are applied and small errors accumulate quickly. In particular, pulse operations in the eight-level system of the $^2F_{7/2}$-manifold are highly sensitive to pulse duration errors, as was shown in Fig. 3.2. A quantitative characterization of the low tolerances in pulse quality for a successful implementation of the GSE sequence in the LLI test is performed in the next section.

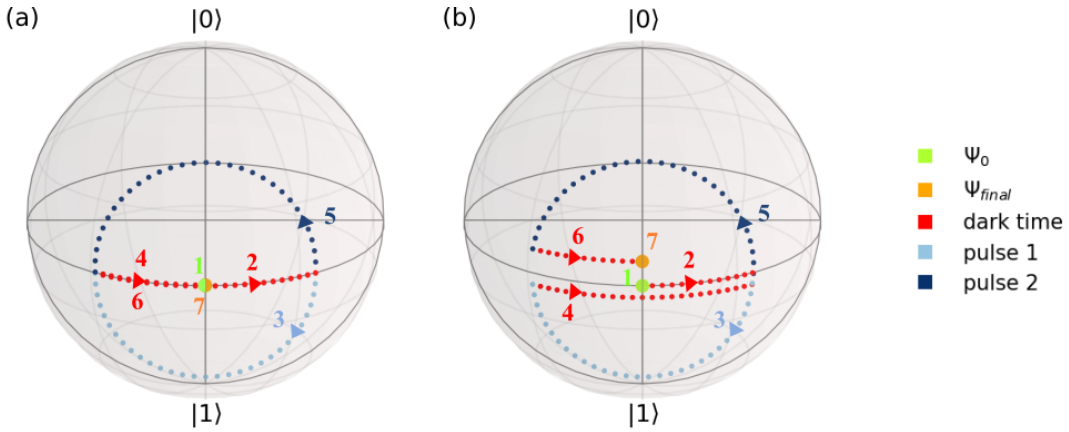

Figure 3.4: Bloch sphere representation of the GSE sequence in a two-level system with two different pulse qualities. (a) shows the evolution of the state throughout the sequence with a detuning of $\delta/\Omega = 3\%$ and no pulse duration error. (b) shows the sequence with identical detuning, but with a pulse duration error of $\Delta t/t_\pi = -3\%$.

While the GSE sequence can only compensate one pulse error type (detuning or duration) at a time, the UR sequences are capable of compensating both types to high degrees simultaneously. In the case of the short UR4 sequence, the compensation mechanisms can both be observed in the Bloch sphere representation shown in Fig. 3.5. The same pulse imperfections of $\delta/\Omega = 3\%$ and $\Delta t/t_\pi = -3\%$ as for the GSE example were assumed. For a clearer visualization, the sequence is split into two images (a) and (b). In order to visually compare the UR4 sequence more closely to the GSE sequece, a common phase of $\pi/2$ was added to all four pulses. The resulting pulses with phases $(1, -1, -1, 1)\pi/2$ only differ in their ordering from two cycles of the GSE sequence. However, this reordering allows the state to shift back towards the equator at the end of the sequence and a high fidelity is reached despite the pulse imperfections.

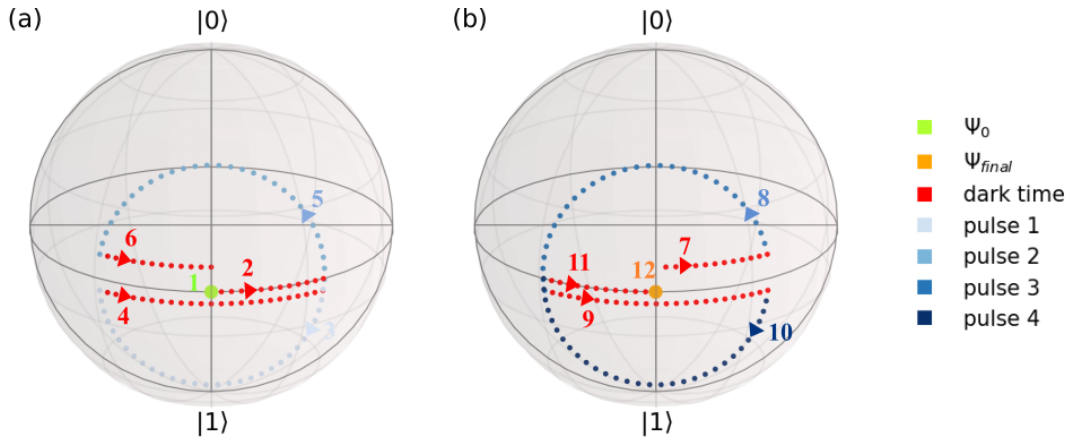

Figure 3.5: Bloch sphere representation of the UR4 sequence in a two-level system with a detuning of $\delta/\Omega = 3\%$ and a pulse duration error of $\Delta t/t_\pi = 3\%$ for all pulses. The sequence is split into (a) and (b) for clearer visualization.

UR10 scheme

While the rephasing mechanisms of the GSE and UR4 sequences can be understood in an intuitive way on the Bloch sphere, the longer URX sequences are too complex for this. Fig. 3.6 shows the state evolution for the UR10 sequence with no pulse errors in (a) and $\delta/\Omega = 0.5\%$, $\Delta t/t_\pi = 2\%$ in (b).

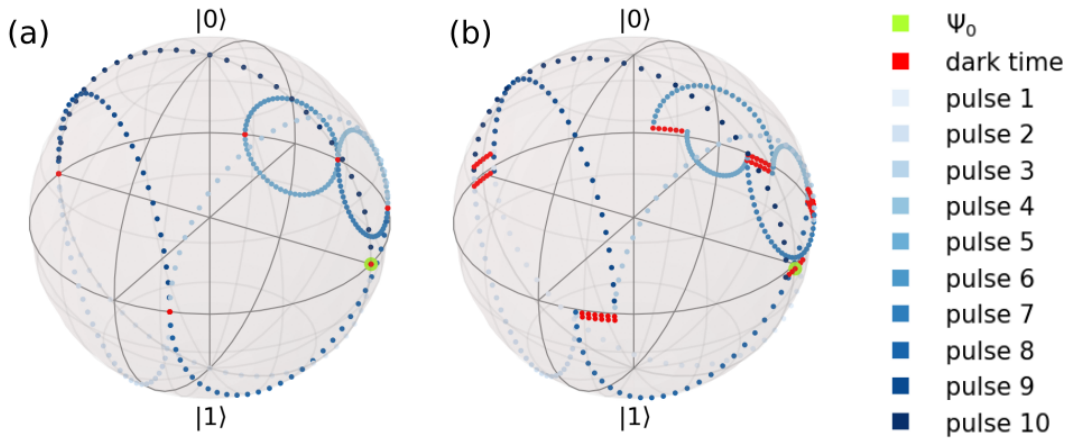

Figure 3.6: Bloch sphere representation of the UR10 sequence in a two-level system with no rf pulse errors in (a) and $\delta/\Omega = 0.5\%$ as well as $\Delta t/t_\pi = 2\%$ in (b). In both cases the initial and final states overlap exactly.

3.5 Numerical robustness analysis

Method

In this thesis, the robustness of a DD scheme refers to its ability to maintain atomic coherence throughout the Ramsey dark time despite rf-pulse errors, namely the detuning δ and duration error Δt. A high robustness is characterized by a high fidelity $\mathcal{F}(\delta, \Delta t)$, which is defined in Eq. 3.8. In order to compare the overall robustness of different schemes, the fidelity of an entire

Ramsey experiment is calculated for a range of errors δ and Δt. The two-dimensional display of $\mathcal{F}(\delta, \Delta t)$ will from now on be referred to as a stability diagram. For an ideal DD scheme, the stability diagram shows a high fidelity in a large region around zero for both types of pulse errors.

In order to calculate a stability diagram for a certain total dark time T_D, the number of DD cycles N_{rep} needed is calculated. Then, the fidelities $\mathcal{F}(\delta, \Delta t)$ are calculated for constant errors δ and Δt throughout the entire Ramsey experiment with N_{rep} cycles. The x- and y-axis of the stability diagram are normalized to the ideal π-pulse duration $t_\pi = \pi/\Omega$ and Rabi frequency Ω respectively, to allow for an easier comparison to different systems.

All stability diagrams in this chapter show fidelities for constant pulse errors throughout the Ramsey experiment. This allows for an easier characterization and comparison of different DD schemes. It is assumed that both the detuning and pulse duration errors only drift slowly compared to the duration of a DD cycle (between 0.43 ms and 2.15 ms) in the experiment. Therefore, DD sequences are also insensitive to temporal variations of δ and Δt, as long as both parameters stay inside a high-fidelity region of the stability diagram.

Robustness of generalized spin-echo sequence

In the initial proposal for the LLI test [14], it was suggested to use the GSE sequence for DD. However, this sequence yielded low coherence times on the order of a few milli seconds in the $^2\mathrm{F}_{7/2}$-manifold, compared to a Ramsey dark time aim of 1 s. The low coherence times achieved with the GSE sequence can be explained by its low robustness against pulse errors.

Fig. 3.7 compares the stability diagrams of the UR10 and GSE sequences applied in the eight-level system of the $^2F_{7/2}$-manifold for $T_D = 1.0$ s, close to the total dark time used for the test of LLI in a single ion [13]. Furthermore, a Rabi frequency of $\Omega/(2\pi) = 33$ kHz and dark time of $t_w = 100$ µs resemble the actual parameters of that experiment. As the GSE diagram shows a ten times narrower error range, it is additionally projected onto the UR10 diagram for an easier scale comparison. It is immediately clear that the UR10 sequence can compensate more than an order of magnitude larger pulse errors than the GSE sequence can in this scenario. While the UR10 sequence achieves high fidelities at any δ/Ω and $\Delta t/t_\pi$ in the ranges $\pm 7\%$ and $\pm 8\%$ respectively, the GSE sequence only yields high fidelities in a small cross shaped area with error ranges of approximately $\pm 0.1\%$ for both error sources. The specific cross shape in the case of the GSE sequence also indicates that it can only compensate one of the error sources at a time, as was already qualitatively shown in the Bloch sphere representation in Fig. 3.4.

Clearly, the UR10 sequence is overall more robust than the GSE sequence for the shown experimental parameters. After the implementation for the LLI test of Dreissen et al. [13], a coherence time of several seconds was observed in the F-manifold. Following this section, the robustness analysis will be extended to the UR16 sequence, as well as even longer dark times to identify a potential improvement for the planned multi-ion test of LLI.

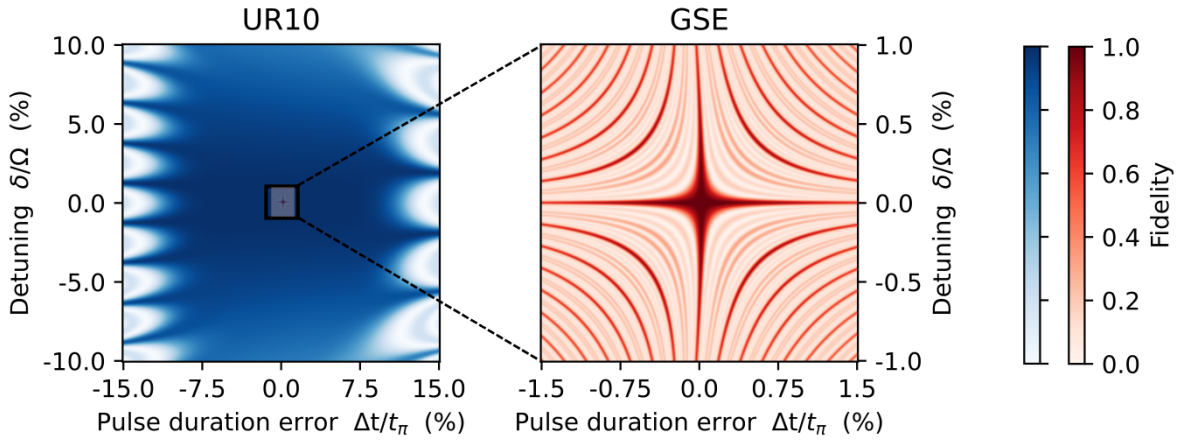

Figure 3.7: Stability diagrams for the UR10 (left) and GSE sequence (right) applied to an eight-level system for a total dark time of $1.0\,\mathrm{s}$. The total dark time, Rabi frequency $\Omega/(2\pi) = 33\,\mathrm{kHz}$ and dark time paramter $t_w = 100\,\mu\mathrm{s}$ were chosen to model the single ion LLI test [13]. For an easier scale comparison the GSE diagram is projected onto the UR10 diagram. It is not a zoom-in panel.

Robustness of UR10 and UR16 as candidates for the multi ion LLI test

It is not clear what limited the observed coherence time of several seconds in the F-manifold in the single ion test of LLI [13]. All experimental sources of error lead to rf pulse imperfections, which can be compensated by a robust DD scheme. Therefore, it is possible that a further extension of the coherence time is possible with the implementation of an even more robust sequence than the UR10 sequence. Furthermore, for the multi-ion test of LLI, additional rf pulse errors can appear from one ion to the next, due to gradients in the applied B-field and driving rf field. The magnitude of these error sources is small compared to the stability region of the UR10 sequence in Fig. 3.7, as will be shown in Chapter 4. However, the addition of these small errors onto those of the single ion case may result in the need for an even more robust DD scheme.

Fig. 3.8 compares the stability diagrams of the UR10 sequence and the longer, more robust UR16 sequence for total dark times of $1.0\,\mathrm{s}$ (left column) and longer dark times (right column). As the stability region of the UR16 sequence is larger, the depicted error ranges are increased compared to the previous Fig. 3.7. In order to quantitatively compare the different scenarios, a high stability region (HSR) will from now on be defined as the region around $\delta = 0$ and $\Delta t = 0$, where $\mathcal{F} \geq 0.85$. For an easy identification of these HSRs, the diagrams display all fidelities ≥ 0.85 in a separate red color map.

At $1.0\,\mathrm{s}$ of Ramsey dark time, it is visible that the UR16 sequence is more robust against pulse duration errors. The HSR is approximately bounded as $-18\% \leq \Delta t/t_\pi \leq 18\%$, where the UR10's HSR only covers $-8\% \leq \Delta t/t_\pi \leq 8\%$. The robustness against detuning is the same for both sequences. Remarkably, it is higher the shorter the pulses are. At $\Delta t = 0$, the HSR spans $-7\% \leq \delta/\Omega \leq 7\%$. This range for the detuning also does not change at longer dark times. As the right column of Fig. 3.8 shows, increased dark time only decreases the robustness against pulse duration errors. At a dark time of $5.0\,\mathrm{s}$, the UR16 HSR spans a range of $-14\% \leq \Delta t/t_\pi \leq 14\%$. This range is significantly higher than the range of the UR10 sequence at a darktime of $1.0\,\mathrm{s}$.

In summary, the UR16 sequence only provides an advantage over the UR10 sequence, if the achieved coherence time is limited by the pulse duration errors. In that case, the UR16 is significantly more robust.

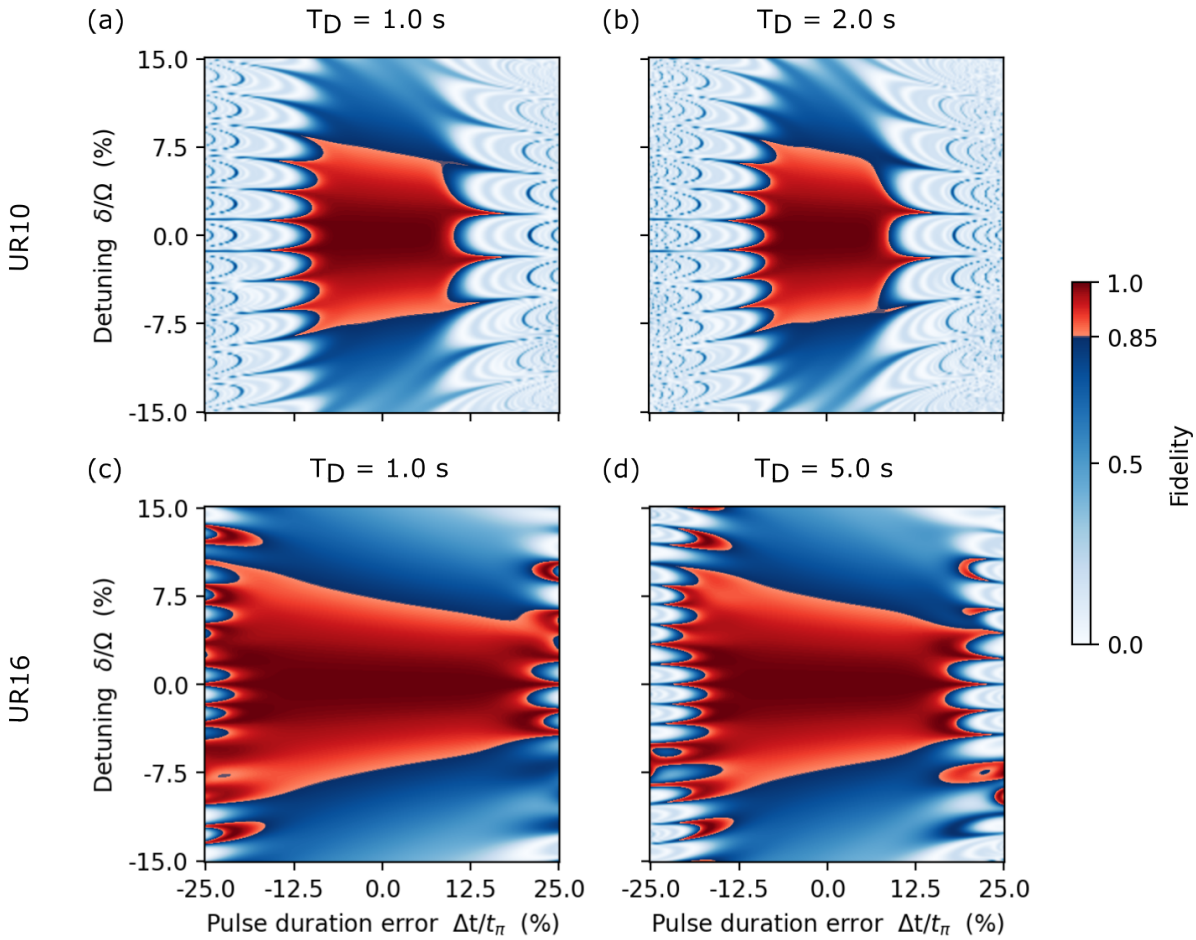

Figure 3.8: Stability diagrams of the UR10 sequence (top row) and UR16 sequence (bottom row) applied to an eight-level system for different Ramsey dark times T_D, as indicated by the titles of the individual diagrams. The Rabi frequency $\Omega/(2\pi) = 33\,\mathrm{kHz}$ and dark time $t_w = 100\,\mu\mathrm{s}$ resemble the parameters of the single ion LLI test [13]. For easier comparison, the high fidelity regions (HFR) with $\mathcal{F} \geq 0.85$ are displayed with a separate red color map.

3.6 Experimental robustness validation in the $^2S_{1/2}$-ground state

In the previous sections, the DD sequences were studied with simulations based on the numerical model presented in Sec. 3.1. Here, the correctness of this model is verified through experimental tests of the stability diagrams. For the GSE and UR10 sequence, the π-pulse duration is scanned at different fixed detunings, producing horizontal cross sections of the stability diagram. This measurement cannot be performed in the $^2F_{7/2}$-state, because the excitation and deexcitation on the E3 transition takes too much time, approximately 50 ms. As a result, the ambient B-field and rf power would drift during the measurement, inhibiting a comparison to the numerical simulation. Therefore, the measurement is performed in the $^2S_{1/2}$-ground state.

Method

As a reference for the experimental tests, a stability diagram is calculated for a two-level system with Ω extracted from Rabi flobs in the $^2S_{1/2}$-ground state. The test is performed with 50 rf pulses and $t_w = 100\,\mu s$, amounting to a total dark time of $T_D = 10\,ms$. In order to verify the correctness of the stability diagram, the experimentally set π-pulse duration is varied at a fixed rf frequency, resulting in a scan of a horizontal line in the diagram. The measured fidelities are compared to a fidelity range extracted from the stability diagram, assuming a B-field drift of approximately 10 µG during the measurement duration of around 5 min for a single scan.

The experimental sequence begins with Doppler cooling of the ion to a temperature of approximately 0.5 mK on the dipole allowed transition near 370 nm. In order to prepare the ion in the initial state of $\left|^2S_{1/2}, m_J = +1/2\right\rangle$, circular polarized 370 nm light is applied with a beam parallel to the quantization axis. As $\kappa = 0$ for the ground state, the ideal outcome of the Ramsey experiment with no rf pulse errors should be again the initial state. The detection of the final state is performed via electron shelving to the $^2D_{5/2}$ state and fluorescence detection on the dipole transition. The narrow laser near 411 nm only excites the $m_J = 1/2$ substate to the $\left|^2D_{3/2}, m_J = 5/2\right\rangle$ state. Therefore, the ion only appears bright during the fluorescence detection if the final state is the $m_J = -1/2$ substate. The experiment is repeated 50 times to obtain measurement statistics. However, as the shelving transition only has an efficiency of about 85%, the probability $P_{-1/2}$ of measuring the $m_J = -1/2$ state only covers the interval [0.15, 1]. To obtain the fidelity of the Ramsey experiment, the measured probability $P_{-1/2}$ is rescaled to the interval [0, 1].

Results for the GSE sequence

The GSE sequence was repeated 25 times to reach the total dark time of 10 ms. Fig. 3.9 (a) shows the corresponding stability diagram with colored horizontal lines representing the experimental scans of the π-pulse duration at four different rf frequencies. The measured fidelities along these lines are displayed in (c), where the color of the measured points corresponds to the color of the respective line in (a). Additionally, the figures in (b) contain the respective fidelity ranges extracted from (a) as gray shaded areas. All four measurements show strong agreement between the calculated and measured fidelities.

Results for the UR10 sequence

The UR10 sequence was repeated five times to reach the dark time of 10 ms. Fig. 3.9 (b) shows the stability diagram with the measurements represented by the colored lines. The measurements along these lines is displayed in (d), where the color of the measurement points corresponds to

the color of the lines in (a). Similarly to the measurement of the GSE sequence, the results show strong agreement with the numerical simulation.

The direct comparison between the measurements of the GSE and UR10 sequence again shows the higher robustness of the latter, especially since the displayed detuning range for the UR10 sequence in (b) is four times larger. The advantage of the UR10 sequence is even stronger when DD is applied in an eight-level system and at longer dark times. In both cases the stability region narrows down more for the GSE sequence than for the UR10 sequence.

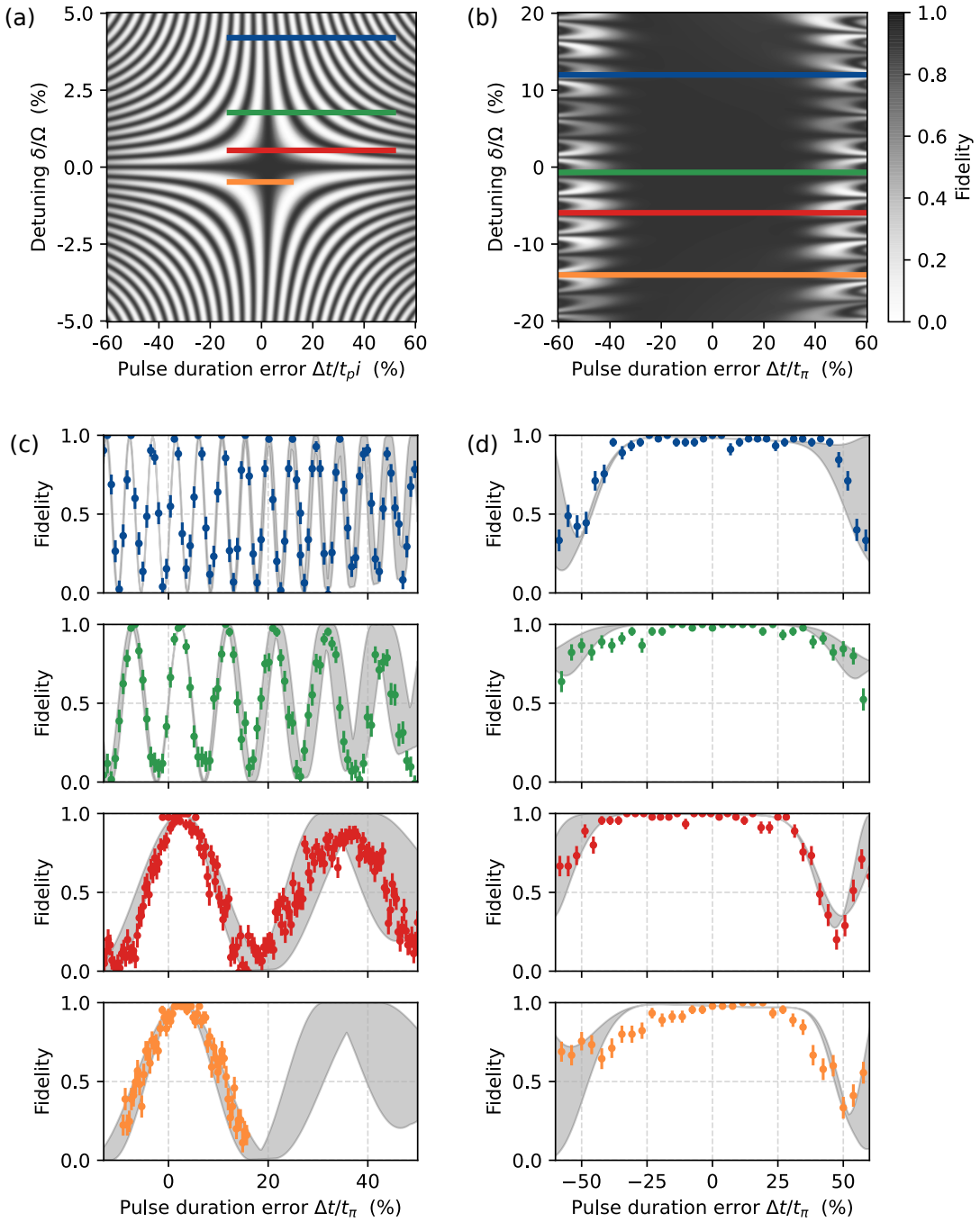

Figure 3.9: Experimental validation of the stability diagram for the GSE and UR10 sequences performed in the $^2S_{1/2}$-ground state with a total dark time of $10\,\mathrm{ms}$. (a) and (b) show the calculated stability diagrams for 25 and 5 repetitions of the GSE and UR10 sequence, respectively, both with $t_w = 100\,\mu\mathrm{s}$. The colored lines represent measurements of the fidelity under varying π-pulse duration for four different rf-frequencies, displayed in (c) and (d) for the GSE and UR10 sequence respectively. There, the colors of the measurement points correspond to the respective lines in the stability diagrams. For both (c) and (d) grey shaded ranges show the simulated fidelity, assuming fluctuations of $10\,\mu\mathrm{G}$ during the measurement duration of $\approx 5\,\mathrm{min}$ for a single scan.

CHAPTER 4

Spatial field homogeneity characterizations

This chapter contains the spectroscopic measurement of both the B-field gradient and the resonant rf field gradient. First, the maximum allowed field gradients allowed for the LLI test are estimated. Both of the fields need to be homogeneous enough over the extent of an ion crystal to allow high enough fidelities of the rf pulse sequence. The maximum allowed B-field gradient is even more stringently bounded by the necessity to efficiently and simultaneously excite all ions via the E3 transition.

Next, the B-field gradient is inferred from a simultaneous measurement of the E2 transition center frequency on six ions in a weakly confined 125 µm long Coulomb crystal. Using a positional shift of one of the B-field coils and a differential current to the coils, a reduction of the measured B-field gradient to (0.00 ± 0.03) µG/µm is demonstrated.

Finally, the resonant rf field gradient is inferred from the measurement of π-pulse durations t_π using simultaneous Rabi flops in the $^2S_{1/2}$ ground state. At t_π deviations of less than 0.7% over the crystal, no minimization of the rf field gradient is necessary.

4.1 Estimation of maximally allowed gradients

Quantization B-field gradient

A gradient of the quantization B-field along the Coulomb crystal of ions has two effects on the experiment. Firstly, the linear Zeeman shift is different for each ion and therefore the E3 transition center frequency ν_0 is slightly different. As the linewidth (FWHM) of this transition is on the order of 10 Hz [18], a small detuning of a few Hertz significantly reduces the excitation probability.

The excitation probability to the $^2F_{7/2}$-state is already reduced due to the limited coherence time during π-pulse excitation and the strong AC-Stark shift, as shown in Ch. 5. Therefore, it is desired that the B-field gradient is reduced to a level, where it is negligible for the E3 excitation efficiency across the crystal. An upper bound for the B-field gradient is set, such that a maximum E3 center frequency shift between the center and outermost ions in a crystal of length 100 µm is less than $\Delta\nu = 1\,\mathrm{Hz}$. With the Zeeman sensitivity of 0.6 Hz/µG for the transition from $m_J = -1/2$ to $m_J = 1/2$ a maximum gradient of

$$\left|\frac{d|B|}{dz}\right|_{\max} = \frac{1}{0.6\,\mathrm{Hz/\mu G}} \cdot \frac{1\,\mathrm{Hz}}{0.5 \cdot 100\,\mu\mathrm{m}} \approx 0.03\,\mu\mathrm{G/\mu m} \tag{4.1}$$

follows[1].

The second effect of the different Zeeman shifts along the crystal is a different rf transition center frequency for the composite pulse sequence in the $^2F_{7/2}$-manifold. The Zeeman sensitivity of the transition between neighboring levels is 1.6 Hz/µG. In section 3.5, the simulations show that a rf detuning within $\delta/\Omega = \pm 5\%$ can easily be compensated by the UR10 sequence, even at a long dark time of 2 s. The Rabi frequency typically lies around 33 kHz in the experiment. Therefore a rf detuning of over 1.6 kHz can be compensated. This B-field gradient requirement is much less stringent compared to the requirement imposed by the E3 transition excitation efficiency.

Rf driving field gradient

A gradient in the intensity of the rf driving field along the Coulomb crystal causes a shift in the Rabi frequency Ω and thus different π-pulse durations t_π. The simulations in section 3.5 show that relative π-pulse duration errors of up to 8% can be compensated by the UR10 scheme. However, it has to be considered that the single ion implementation of the sequence already showed the necessity of a robust scheme. Therefore, temporal variations of the rf intensity occur as well. Additional spatial variations caused by an intensity gradient of the rf driving field should be smaller. As a conservative requirement, a maximum spatial variation of t_π along the crystal of 1% is considered.

4.2 Quantization B-field gradient

The experiment's quantization B-field is set with a pair of coils aligned along the H2 beam, as indicated in the cross section drawing in Fig. 4.1. The distance between the coils is higher than the distance in a Helmholtz configuration. Therefore, the B-field strength is not homogeneous along the H2 beam, but decreases towards the center of the coils. As the angle between the

[1] Here the z-direction refers to the trap axis. This is in contrast to Ch. 2, where it is the direction of the quantization B-field.

H2 beam and the trap axis is small, the B-field strength behaves similarly along the trap axis, showing a minimum where the trap axis crosses the central plane between the coils. Because the length of a ten ion Coulomb crystal, $\approx 100\,\mu m$, is small compared to the distance between the coils, the curvature of the field strength is negligible. To minimize the local linear B-field gradient, the B-field minimum has to overlap with the trapping region.

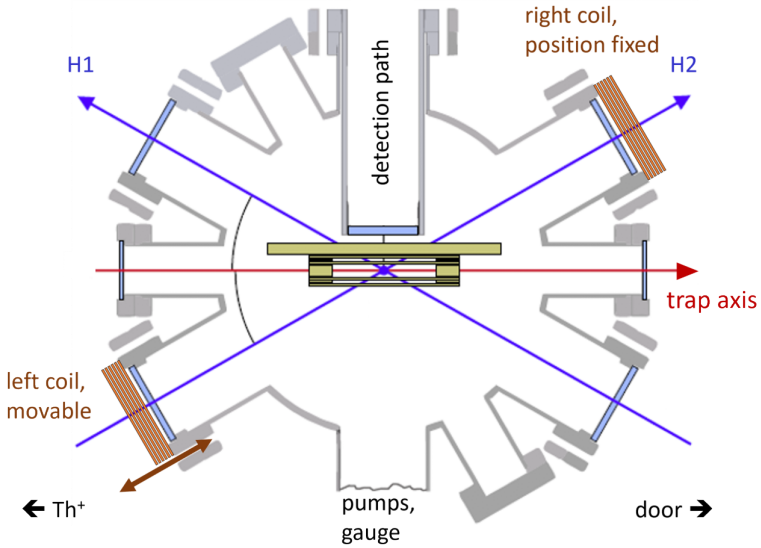

Figure 4.1: The experiment's geometry from a top view, modified figure from ref. [21]. The quantization B-field is generated by two coils aligned along the H2 beam. The left coil can be moved back and forth by a few millimeter, while the right one is fixed. The trap axis is displayed in red.

Measurement method for B-field gradient

In order to directly measure the B-field gradient in the trapping region, spectroscopy on a Coulomb crystal of ions is used. A simultaneous measurement on all ions of the crystal has the advantage that temporal B-field drifts don't influence the result. For each ion, the center frequency of a Zeeman sensitive transition is measured. The frequency shifts along the crystal quantify the local B-field gradient. The narrower the used transition is, the more accurate the extracted center frequencies. However, the very narrow E3 transition is not well suited, because in addition to the Zeeman shift, the large AC-Stark shift can vary along the crystal. Therefore the E2 transition from the $^2S_{1/2}$ ground state to the $^2D_{5/2}$ state was used. The driving 411 nm beam has a waist of $w = 83\,\mu m$ and can illuminate an entire Coulomb crystal. At low optical power, Fourier limited transition linewidths of around 800 Hz can be achieved, which are sufficiently narrow to characterize the B-field gradient. A high Zeeman sensitivity of 2.8 MHz/G is achieved with the transition from $m_J = \pm 1/2$ to $m_J = \pm 5/2$.

For all measurements of the B-field gradient in this chapter, a Coulomb crystal of six ions with low axial confinement was used. The total length of the crystal was measured to be 125 µm, using the distance of the fluorescence peaks on the EMCCD chip and a magnification factor of 24 of the imaging setup [22]. The ions are first cooled to Doppler temperature and then optically pumped to the $|S, m_J = -1/2\rangle$ state. Then a π-pulse of 411 nm light is applied, followed by flourescence detection on the dipole transition near 370 nm.

Each spectrum was measured by scanning the laser frequency with a doublepass AOM in steps of 100 Hz and repeating the measurement 200 times at each frequency. A typical spectrum

for all six ions is shown in Fig. 4.2. As the absolute transition frequency is irrelevant for the calculation of the B-field gradient, the laser frequency is subtracted by a common offset. The ions are labelled from 1 to 6 (leftmost to rightmost in Fig. 4.1). The depicted error bars represent the quantum projection noise. The different maximum excitation probability of each ion is caused by the Gaussian beam profile of the 411 nm beam causing different Rabi frequencies for each ion. For all spectra used in this chapter, the measurement contrast for all ions was at least 50%. Fig. 4.2 also contains a fit of the measured spectral lines. As a fit function a Gaussian of the form

$$P_e(\nu) = P_0 \cdot exp\left(-\frac{(\nu-\nu_0)^2}{2\sigma^2}\right), \tag{4.2}$$

was used, with the excitation probability P_e and laser frequency ν. The fit parameters are the maximum excitation probability P_0, transition center frequency ν_0 and 1/e linewidth σ. As only the fitted center frequency is of interest, the Gaussian function was chosen for easier handling in the fitting process, instead of the physically correct model for excitation with a rectangular π-pulse.

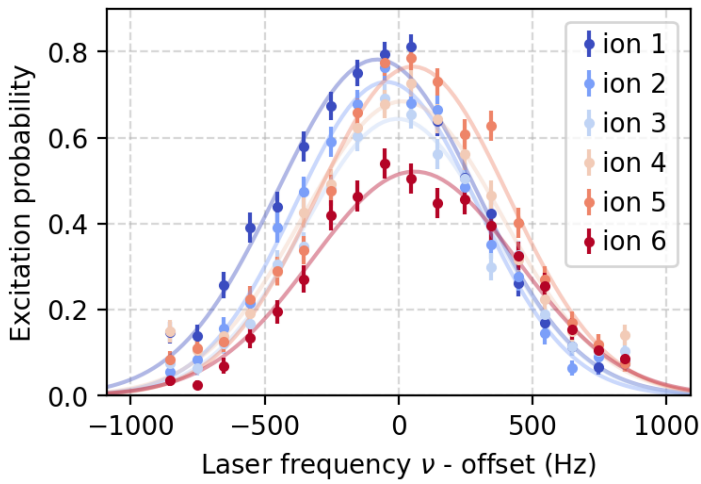

Figure 4.2: Typical spectra of the $^2S_{1/2}$ to $^2D_{5/2}$ transition, measured simultaneously on six ions in a Coulomb crystal. For each point the average of 200 measurements is taken and the error bars show the quantum projection noise. To extract the center frequency of each spectral line, a Gaussian fit of Eq. 4.2 is used.

The six different transition frequencies ν_0 obtained from the measured spectra are used to calculate a B-field gradient. Fig. 4.3 shows the fitted center frequencies of the spectra in Fig. 4.2 plotted over the respective ion's position as blue points. To reduce the effect of statistical deviation, a second spectrum is measured and the center frequencies displayed in red. Each fitted center frequency ν_0 is displayed with an error bar representing the error obtained by the Gaussian fit. The results from both spectra in Fig. 4.3 agree well and show a clear linear dependence of ν_0 on the ion's position along the trap axis. A combined linear fit of $\nu_0(z)$ results in a slope of $(1.28 \pm 0.06)\,\mathrm{Hz/\mu m}$, where the uncertainty is the fit error of a weighted fit considering the uncertainties of the individual transition frequencies. From this slope, the B-field gradient can be calculated using the Zeeman sensitivity as

$$\frac{d|B|}{dz} = \frac{1}{2.8\,\mathrm{Hz/\mu G}} \cdot \frac{d\nu_0}{dz}. \tag{4.3}$$

The resulting gradient is (0.44±0.02) µG/µm. In the following sections, two methods for reducing the B-field gradient at the crystal's position are presented. Each measurement of the gradient is performed using exactly the same method as is described in this section.

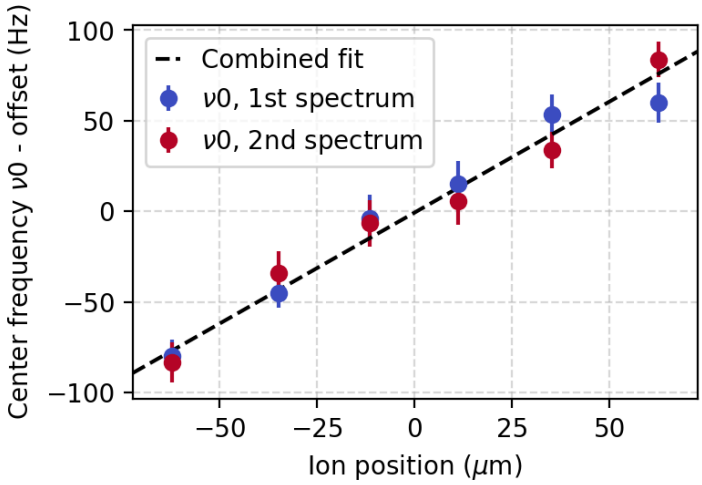

Figure 4.3: The fitted center frequencies obtained in two measurements over the respective ion's position. The error bars represent the uncertainties obtained by a fit of the respective spectra. As only the frequency gradient along the crystal is of interest, a common frequency offset is subtracted from each of the two measurements.

Reduction of gradient via the coil position

A reduction of the B-field gradient was achieved by both repositioning one of the coils and moving the ion crystal within the trapping segment. Fig. 4.4 shows the measured gradients after both of the described adjustments. The x-axis gives the position of the crystal's center along the trapping axis in respect to the usual trapping location close to the center of the 2 mm long segment. The three different point colors in the plot represent three different positions of the left B-field coil in Fig. 4.1. At the initial coil position the crystal was shifted 382 µm to the left and 378 µm to the right by changing the DC voltages of the trap electrodes confining the crystal axially. The distances were measured by comparing the initial and final position of the fluorescence peaks on the EMCCD camera. Within this position range, the B-field gradient was tuned between (-0.22 ± 0.02) µG/µm and (-0.13 ± 0.02) µG/µm.

With the crystal positioned at the center of the trapping segment, the position of the B-field coil was moved two times. First the coil was pulled away from the chamber by a few millimeters. This changed the gradient from (-0.15 ± 0.03) µG/µm to (0.08 ± 0.02) µG/µm. Afterwards the coil was pushed back towards the chamber, yielding a gradient of (-0.06 ± 0.02) µG/µm.

In summary, moving the ion crystal within the trapping segment does not provide a large enough tuning range and is impractical, because it requires a realignment of all laser beams. Moving the left coil in Fig. 4.1 allows for a large enough tuning range to move the B-field minimum across the ion crystal. However, the placement of the coil by hand is not accurate enough to reduce the gradient to below the threshold of 0.03 µG/µm. This method should only be used for a rough initial minimization followed by fine adjustments with the current thief method presented in the next section.

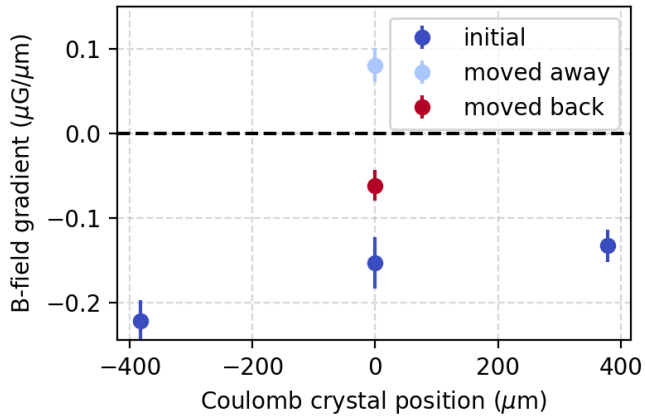

Figure 4.4: Measured B-field gradients at different positions along the trapping axis within the 2 mm segment (indicated by the x-axis) and different positions of the left B-field coil in Fig. 4.1 (indicated by the point colors).

Reduction of gradient using a current thief

A fine adjustment of the B-field gradient to below the set threshold of 0.03 µG/µm was achieved by implementing a tunable differential current between the two B-field coils. The differential current is set by adding a voltage-controlled resistance (current thief) in parallel to the left B-field coil, as indicated in Fig. 4.5 (a). The current thief can take control-voltages U_t between 0 V and 5 V. Fig. 4.5 (b) shows the measured B-field gradient at five different applied values of U_t. The gradient response is linear around the central value $U_t = 2.5\,\mathrm{V}$ and saturates towards the edges of the tuning range. A movement of the coil during the attachment of the current thief by chance caused a reduction of the gradient to (0.00 ± 0.03) µG/µm when $U_t = 0\,\mathrm{V}$ is applied. At $U_t = 5\,\mathrm{V}$, the gradient was measured to be (0.50 ± 0.02) µG/µm.

Using the current thief allows to finely minimize the B-field gradient. The accuracy of this method is only limited by the accuracy of the gradient measurement method using spectroscopy of the E2 transition. Ideally, the coil should be positioned, such that a zero B-field gradient is achieved in the linear tuning range around $U_t = 2.5\,\mathrm{V}$. For the multi-ion E3 excitation presented in Ch. 5 the B-field gradient was minimized again. There, the coil was positioned in the ideal way and a fine scan of the gradient was performed in the linear range around $U_t = 2.5\,\mathrm{V}$. The result is presented in Sec. 5.4.

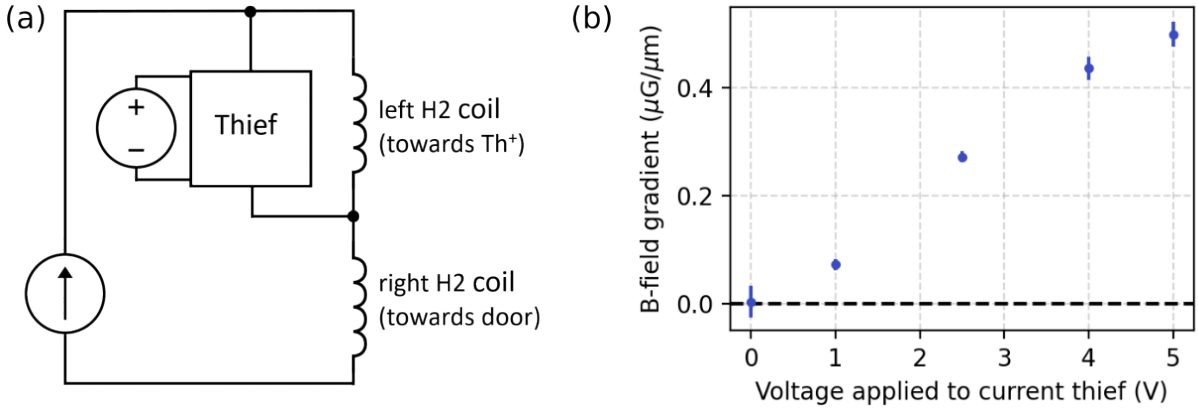

Figure 4.5: Schematic circuit diagram of the current thief placement (a) and measured B-field gradients at different control voltages of the current thief (b).

4.3 Transition driving rf field gradient

The gradient of the transition driving rf field was measured with a 125 µm six ion crystal as well. Rabi flops between the two Zeeman sublevels of the $^2\mathrm{S}_{1/2}$ ground state were used to determine differences in the Rabi frequency along the crystal.

The ions were Doppler cooled and optically pumped to the $\left|^2S_{1/2}, m_J = -1/2\right\rangle$ state. Then, the resonant rf field was applied for varied times up to 5.2 ms, driving Rabi flops between the $m_J = -1/2$ and $m_J = +1/2$ Zeeman sublevels. The detection of the final state was achieved by shelving the $\left|^2S_{1/2}, m_J = -1/2\right\rangle$ state to the $\left|^2D_{5/2}, m_J = -5/2\right\rangle$ state and performing fluorescence detection on the $^2\mathrm{S}_{1/2}$ to $^2\mathrm{P}_{1/2}$ transition. If an ion appears dark during the detection, it was in the $\left|^2S_{1/2}, m_J = -1/2\right\rangle$ state after the rf field application. Because of the limited waist $w = 83\,\mu\mathrm{m}$ of the 411 nm beam, shelving could not be efficiently performed for all ions with the same π-pulse duration. Instead, a long 15 ms laser pulse was applied, during which decay to the long lived $^2\mathrm{F}_{7/2}$ state takes place with a large probability. This method resulted in a more uniform shelving efficiency between 70% and 80% across the crystal.

The final 200 µs of the total 5.2 ms of Rabi flops are shown in Fig. 4.6 (a). Due to the finite shelving efficiency, the measured excitation probabilities do not drop below 20%. The limited maximum excitation probabilities between 80% and 90% are caused by inefficient optical pumping, partly caused by the finite waist and non-central alignment of the H2 370 nm beam. It was not possible to perform a fit with the model function on the entire 5.2 ms of Rabi flops. Instead, only the displayed last 200 µs were fitted, where a small phase shift between the sine-oscillations has accumulated. The measured data was fitted according to

$$P_e(t) = P_{\max} \sin\left(\frac{\pi t}{2t_\pi}\right)^2 + P_0, \tag{4.4}$$

with fitting parameters $P_{\max}$, P_0 and π-pulse duration t_π.

In Fig. 4.6 (b) the relative deviation $\Delta t_\pi / \langle t_\pi \rangle$ of the fitted π-pulse durations to the average over the crystal $\langle t_\pi \rangle$ is plotted over the respective ion position. The error bars represent the fit uncertainty, covering a range of $-0.7\% < \Delta t/t_\pi < 0.6\%$. This range is well within the set threshold of $\pm 1\%$ of π-pulse duration errors across the crystal. Therefore, a minimization of the rf field gradient is not necessary. Furthermore, the measured range of π-pulse duration deviations is dominated by the uncertainty of the fitting procedure. A more precise measurement of the individual π-pulse durations would likely yield less deviation.

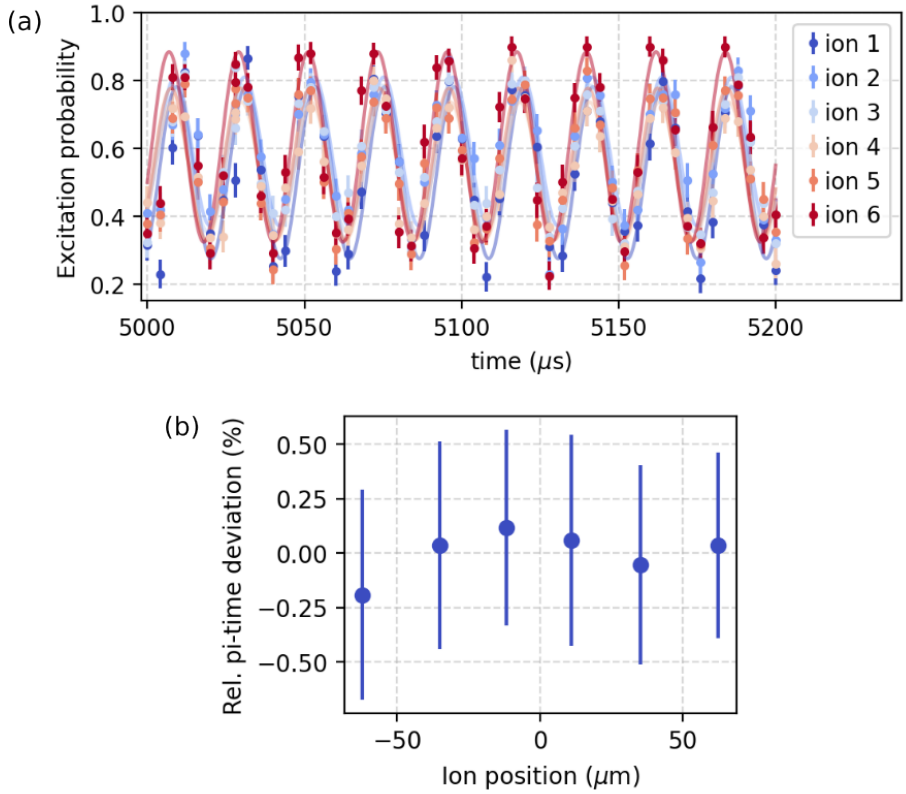

Figure 4.6: Measurement of the homogeneity of the transition driving rf field. (a) shows the last 200 µs of a total 5.2 ms of Rabi flops between the two Zeeman levels of the $^2S_{1/2}$ ground state. During this time only a small phase offset has accumulated between the Rabi flops of the individual ions. The measured data is fitted using Eq. 4.4 and the deviation of the extracted π-pulse durations are shown in (b) over the respective ion position.

CHAPTER 5

Coherent excitation of a Coulomb crystal to the ^{2}F-state$_{7/2}$

The simultaneous coherent E3 excitation with high population transfer of all ions in a Coulomb crystal is essential to a successful multi-ion LLI test. This chapter contains the progress made towards the excitation of ten ions, from the design of the interrogation laser profile to the successful simultaneous excitation of six ions.

First, the large measured AC-Stark shift is considered to calculate a requirement of the interrogation laser field uniformity over the ion crystal. To meet the requirement of less than $\pm 2\%$ laser intensity variation and efficiently use the available laser power, a focussed line-shaped top-hat beam profile is produced with a custom designed phase plate. The optical setup is introduced and the uniformity of the beam profile is measured with a high-resolution beam profiling camera. A highly uniform section of the profile is used to excite a linear eight ion crystal, resulting in the successful simultaneous excitation of six ions at the same transition frequency.

5.1 AC-Stark shift and beam homogeneity requirements

For simultaneous coherent excitation to the $^2\mathrm{F}_{7/2}$ state, all ions need to be driven with the same Rabi frequency at the same E3 transition frequency. The most limiting effect is the strong AC-Stark shift of $\Delta\nu_{\mathrm{AC}} \approx 440\,\mathrm{Hz}$ at a typical intensity of the interrogation laser field leading to a π-pulse duration of $t_\pi = 50\,\mathrm{ms}$ [18]. Different laser field intensities at each ion position lead to different AC-Stark shifts larger than the Fourier limited linewidth (FWHM) of $\Delta\nu_{\mathrm{Fourier}} \approx 17\,\mathrm{Hz}$ for π-pulse excitation at the previously assumed laser intensity. The relation between AC-Stark shift frequency and corresponding Fourier-limited linewidth

$$\Delta\nu_{\mathrm{AC}} = (0.66 \pm 0.06)\,\mathrm{Hz}^{-1}\,\Delta\nu_{\mathrm{Fourier}}^2 \tag{5.1}$$

was measured in ref. [18]. It is used in the following to calculate the reduced excitation probabilities of ions in a crystal for different intensity variations to obtain requirements on the beam homogeneity.

The excitation probabilities are calculated with the Lindblad equation solver provided by the Python package *QuTiP*. The Lindblad equation

$$\partial_t \rho = -\frac{i}{\hbar}\,[\mathcal{H}, \rho] + \sum_j \left(c_j \rho c_j^\dagger - \frac{1}{2}\rho c_j c_j^\dagger - \frac{1}{2} c_j c_j^\dagger \rho \right) \tag{5.2}$$

is used here to model the time evolution of the density matrix ρ for the two-level system composed of the $^2\mathrm{S}_{1/2}$ ($|0\rangle$) and $^2\mathrm{F}_{7/2}$ ($|1\rangle$) states. The total Hamiltonian

$$\mathcal{H} = \mathcal{H}_{\mathrm{atom}} + \mathcal{H}_{\mathrm{interaction}} = 2\pi\nu_{\mathrm{AC,diff}}\,|1\rangle\langle 1| + \frac{1}{2}\Omega\,(|1\rangle\langle 0| + |0\rangle\langle 1|) \tag{5.3}$$

accounts for the differential AC-Stark shift of an ion compared to the average AC-Stark shift over all ions of a Coulomb crystal and the intensity dependence of the Rabi frequency Ω on intensity variations compared to the average intensity over the crystal. For this calculation, only a single collapse operator $c = \sqrt{\Gamma}\,|0\rangle\langle 0|$ is considered, accounting for the measured decoherence time $\tau = (190 \pm 27)\,\mathrm{ms}$ during the interaction [18].

The quantity of interest is the excitation probability of an ion that is illuminated with intensity $I = I_{\mathrm{av}} + \Delta I$ compared to the average intensity I_{av} after the average π-pulse duration t_π. This quantity is shown in Fig. 5.1 for four different π-pulse durations. With the highly focused Gaussian beam used for single ion excitation, π-pulse durations of 50 ms can be achieved [18]. At this high intensity the decoherence limited maximum excitation probability is $\approx 90\%$. Due to the large AC-Stark shift at this high intensity, the excitation probability drops off quickly with $|\Delta I / I_{\mathrm{av}}|$, which induces a detunig to the transition. For lower intensities and thus longer pulse durations, the maximum excitation probability decreases, but the drop-off with intensity variations is less severe.

In order to gain significant sensitvity to LV in a multi-ion LLI test, the measurement contrast should stay as high as possible for all ions in the crystal. Therefore, a goal of at least 80% excitation probability on the E3 transition is set for all ions. From Fig. 5.1 it is apparent, that π-pulse durations of less than 100 ms have to be achieved, as decoherence becomes limiting otherwise. For sensible π-pulse durations between 70 ms and 80 ms, the laser intensity may not vary more than $\pm 2\%$ over the entire ion crystal to maintain at least 80% excitation for all ions.

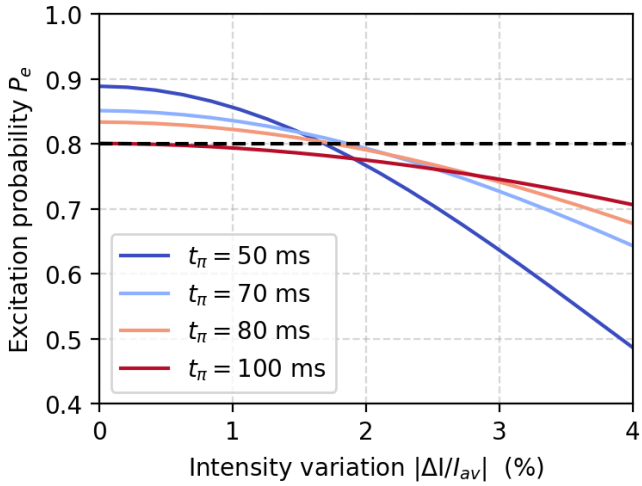

Figure 5.1: Calculated maximum excitation probability on the E3 transition with π-pulses of different duration t_π over a relative laser intensity variation, causing a detuning via the AC-Stark shift. The excitation probabilities are calculated by solving the Lindblad equation numerically and assuming measured values for achievable π-pulse durations, and corresponding AC-Stark shifts [18].

5.2 Beam shaping method

Beam shaping device

A holographic phaseplate is used to transfer a Gaussian input beam (TEM00) into a focussed line-shaped beam profile with a uniform intensity distribution along the center of the profile. A line-shaped profile is chosen over standard square or circular top-hat profiles to efficiently use the available laser power along the linear Coulomb crystal. The phaseplate is a custom designed diffractive optical element (DOE) provided by *HoloOr* [1]. It is a 1″ fused silica plate with a micro-structured pattern that diffracts the input light into the desired profile at a fixed working distance of WD = 550 mm. The DOE is designed to produce a 250 µm long line that has a diffraction limited Gaussian profile with waist $w = 33$ µm in the transversal direction. The 250 µm length of the line profile describes the $1/e^2$-length, corresponding to a region of ≈ 150 µm with intensity variations below 2% at the center of the line. For a sensitve LLI test with ten ions, the linear Coulomb crystal needs to have a length of ≈ 100 µm. To obtain the desired intensity profile, the collimated Gaussian input beam has to fulfill the exact design criteria, which are a waist of $w = 2.5$ mm and an M^2-value as close to 1 as possible.

[1] For future purchases of the same DOE design, the sales opportunity number IN22016775 can be referenced.

Test setup

The intensity distribution of the shaped flat-line beam was characterized with a high resolution beam profiling camera in a test setup depicted in Fig. 5.2. The main optical components are the same as used for the setup pointing to ions.

First, the light is delivered with a single mode polarization maintaining optical fiber with FC/APC-connectors. The fiber is used as a mode cleaning device, delivering a nearly perfectly shaped Gaussian beam profile. A large beam fiber outcoupler (Thorlabs, C20APC-A) is chosen, so that the exiting beam with a waist of $w \approx 1.9\,\mathrm{mm}$ can directly be expanded to the required $w = 2.5\,\mathrm{mm}$ with the following telescope. Additionally, Thorlabs promises a high Gaussian beam quality with M^2-values close to one, due to the air spaced lens design. The variable telescope (Thorlabs, ZBE2A) offers continuous beam expansion between 1x and 4x and tunable collimation correction. Both of these degrees of freedom had a large impact on the quality of the final shaped beam, making the variable telescope an indispensable component of the setup.

The holographic phaseplate is aligned with a 6-axis kinematic mount (Thorlabs, K6XS) on top of a translation stage. Tests of all the degrees of freedom showed, that the x- and y-positioning of the phaseplate is more crucial than the tilt settings. A careful manual placement of the phaseplate mount and the telescope in respect to each other suffices for low enough tilt. The translation stage can be used to move the phaseplate along the beam propagation direction, allowing for fine control of the beam focus position. During the alignment procedure with the test setup, and later on while aligning the beam onto the ions, it proved more convenient to use the tunable collimation correction of the telescope to slightly move the focal position of the beam. Using the translation stage introduces a slight beam walk-off, because the stage does not move perfectly collinear with the beam direction. Finally, the rotation setting of the mount is important to define the orientation of the line shaped beam profile along the ion crystal.

A high resolution beam profiling camera (Ophir, 3.69 µm effective pixel size) is placed 550 mm after the phaseplate at the specified focal position. The most uniform intensity distribution recorded with the camera is shown in the next section.

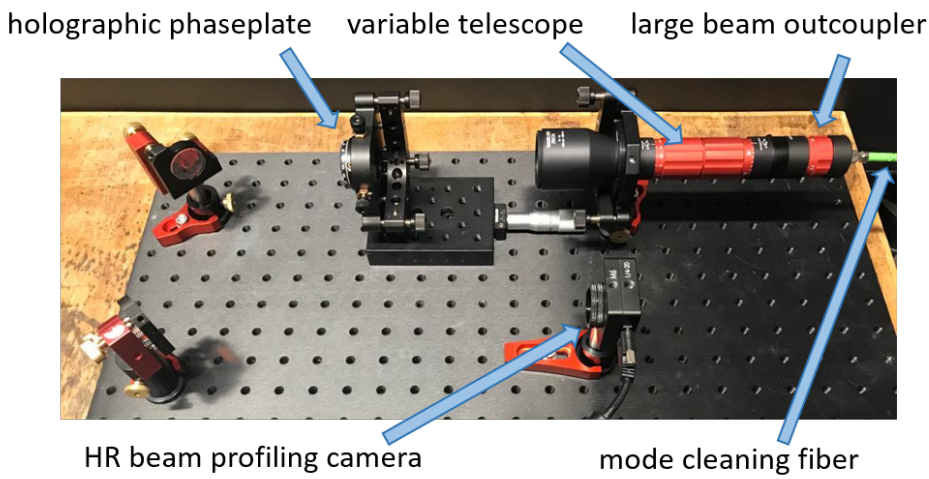

Figure 5.2: Test setup for the characterization of the shaped flat-line profile using a high resolution beam profiling camera.

5.3 Beam shaping results

Flattest line profile achieved

Using the test setup, all alignment degrees of freedom were thoroughly tested. The recorded profile with the most homogeneous intensity distribution is shown in Fig. 5.3. It does not fully match the design criteria. However, the intensity distribution in a region of the beam is flat enough to be used for excitation on the E3 transition. Additionally, the observed imperfection can be attributed to noise in the Gaussian intensity profile, used to illuminate the phaseplate. Therefore it is likely that the phaseplate itself perfectly matches the specifications.

Fig. 5.3 (a) shows the full recorded intensity profile. For a more detailed characterization, vertical and horizontal cut-throughs of the profile are shown in (b) and (c) respectively. The cut-throughs are obtained by extracting the values from a single column/row of pixels from the camera image. In the vertical direction, the beam exhibits a close to perfect Gaussian profile with a fitted waist of $w = 33.5\,\mu\text{m}$. This agrees well with the diffraction limited spot size $w = 33\,\mu\text{m}$ of a Gaussian beam with a waist of $w = 2.5\,\text{mm}$ at a focal distance of $550\,\text{mm}$.

The horizontal cut-through in Fig 5.3 (c) shows a flat intensity distribution on the right side, which is magnified in the zoom-in panel. Here it can be seen that the intensity variation is less than $\pm 2\%$ of the average over a distance of approximately $80\,\mu\text{m}$. This region of the beam is well suited for the E3 excitation of Coulomb crystal with that length. The left side of the beam features a peak and a dip, where the intensity varies by a maximum of +11% and -9% in respect to the average intensity of the flat section. Therefore, the left side cannot be used for E3 excitation. The imperfection of the profile was found to be caused by the Gaussian beam illuminating the phaseplate. When the phaseplate is rotated by 180° in its mount and the beam is realigned, the imperfection is still located on the left side of the shaped profile. However, when the attached system of fiber outcoupler and telescope is rotated by 180°, a mirrored version of the shaped profile is observed on the camera image, wtih the peak on the right side. A characterization of the Gaussian profile exiting the telescope is performed in the next section.

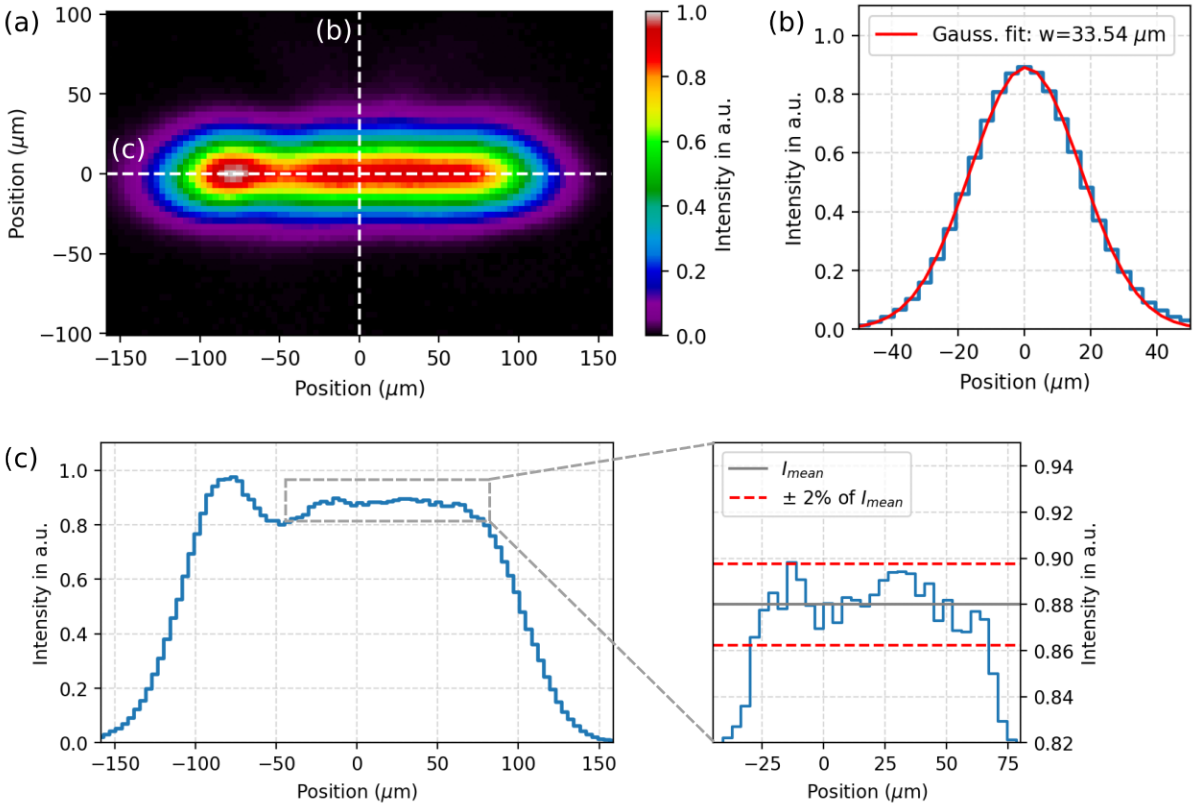

Figure 5.3: Measured intensity distribution of the shaped flat-line profile using the test setup of Fig. 5.2. (a) shows the full 2D-profile with white dashed lines indicating the location of a horizontal and vertical cut-through. (b) shows the vertical cut-through with a Gaussian fit. (c) shows the horizontal cut-through with a zoom-in panel of the flat intensity region.

Spatial noise on Gaussian input beam

As the imperfection in the shaped line profile can be attributed to noise in the beam illuminating the phaseplate, a further investigation of the Gaussian profile was performed with the beam profiling camera. The camera was placed at the output end of the telescope in the test setup and the magnification and collimation settings of the telescope were set to the values that produced the line profile in Fig. 5.3. The measured intensity profile is depicted in Fig 5.4, where (a) shows the full 2D-profile and (b) and (c) show the central horizontal and vertical cut-throughs respectively, along with Gaussian fits according to

$$I(x) = I_0 \cdot \exp\left(\frac{-2\,(x - x_0)^2}{w^2}\right). \tag{5.4}$$

It can be observed, that the fit functions differ considerably from the recorded intensity distributions, which include high-frequency spacial noise around the peak and fall off slower at the edges. In addition, the fitted waist in the horizontal direction $w_h = 2.19\,\mathrm{mm}$ is much smaller than the waist in the vertical direction $w_v = 2.49\,\mathrm{mm}$, the latter being very close to the specified waist for the phaseplate $w = 2.5\,\mathrm{mm}$. It is unclear which of the imperfections in the Gaussian beam cause the peak in the shaped line profile, so further investigations are necessary. An explanation for the two different waists could be an angle mismatch between the fiber tip of the FC/APC connector and the lenses in the fiber outcoupler, inducing comatic aberration. Therefore it could be useful to test the system with an unangled FC/PC fiber and outcoupler.

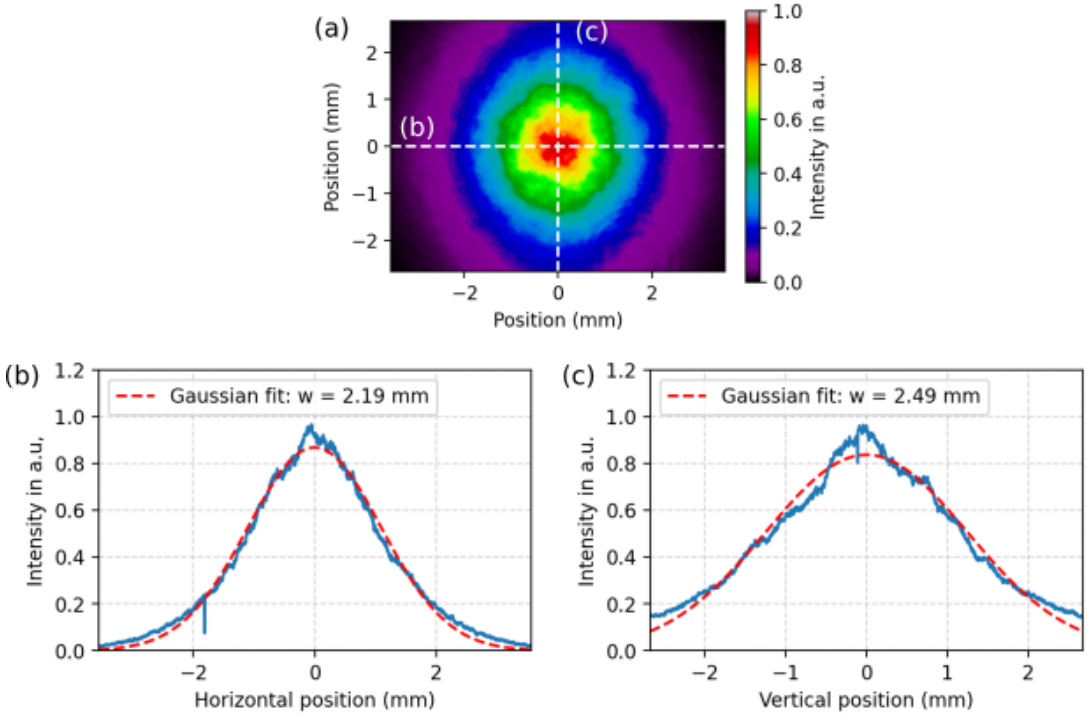

Figure 5.4: Measured beam profile at the exit of the telescope set to the magnification and collimation values used to achieve the line profile in Fig. 5.3. (a) shows the full measured profile, where the frame size is limited to the chip size of the camera. (b) and (c) show central horizontal and vertical cut-throughs respectively, along with Gaussian fits according to Eq. 5.4.

5.4 Coherent E3 excitation in a Coulomb crystal

Beam alignment process

The process of aligning the shaped line profile of the 467 nm beam to the linear ion Coulomb crystal is challenging, because in addition to the lateral pointing also the precise focal distance and the correct angular orientation of the phaseplate need to be found. It is not feasible to use the E3 excitation directly as a feedback during alignment, because the AC-Stark shift causes a frequency shift of several transition linewidths, depending on how well the beam overlaps with the ions. Therefore, the alignment was done while performing spectroscopy on the E2 transition from the $^2S_{1/2}$ to the $^2D_{5/2}$ state and monitoring the AC-Stark shift induced by the 467 nm light on it. An eight-ion crystal of $\approx 80\,\mu$m length was used to infer the intensity distribution of the beam along the trapping axis.

For the measurement of the AC-Stark shift to the E2 transition $\nu_{\mathrm{AC},411}$, two Rabi frequency scans were taken in an interleaved fashion. During one scan the 467 nm light was switched off and during the other scan it was switched on. The E2 interrogation beam power was highly attenuated, leading to 2.0 ms π-pulses and narrow transition linewidths (FWHM) of ≈ 650 Hz. Fig. 5.5 (a) shows an exemplary measurement of the two frequency scans along with Gaussian fits of each transition. The difference of the fitted center frequencies corresponds to the AC-Stark shift $\nu_{\mathrm{AC},411} = (423 \pm 18)$ Hz.

This described measurement is simultaneously performed on all ions of the crystal. Through an iterative process of adjusting the alignment parameters and measuring the AC-Stark shift,

a uniform intensity distribution was reached. Fig. 5.5 (b) shows the corresponding fitted AC-Stark shifts for all ions over the respective ion positions. The lowest and highest value differ by -4% and +3%, respectively, from the average over the crystal. Especially the crystal section between the third and seventh ion from the left shows a highly uniform AC-Stark shift.

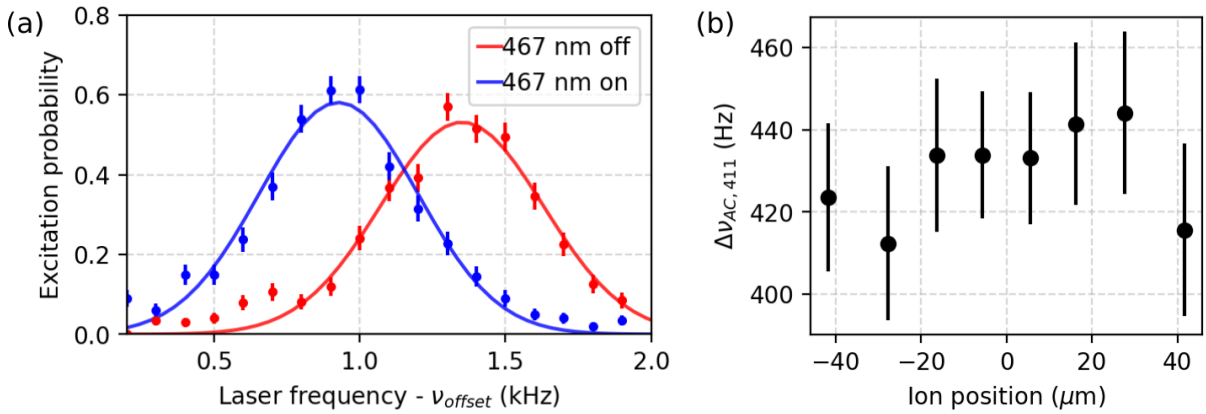

Figure 5.5: Measurement of the AC-Stark shift induced by the 467 nm laser beam onto the E2 transition. (a) exemplarily shows two interleaved Rabi frequency scans of the E2 transition, with the 467 nm light switched on and off, for the leftmost ion in the crystal. The transitions are fitted with Gaussian curves and the transition center frequencies are extracted, yielding the shift. (b) shows the AC-Stark shift for all ions over the respective ion position.

Successful multi-ion excitation

Using the 467 nm beam alignment corresponding to the uniform measured AC-Stark shifts shown in Fig. 5.5 (b), a simultaneous coherent excitation of the eight ion Crystal was achieved.

The characterization of the magnetic field gradient had been performed months before this measurement and the quantization B-field coils were likely moved while working on the optics surrounding the experimental chamber. Therefore, another scan of the B-field gradient at different current thief voltages was taken using the $\approx 80\,\mu\text{m}$ long eight ion crystal, following the same procedure as outlined in Sec. 4.2. The result is shown in Fig. 5.6. The smaller length of this crystal resulted in larger measurement uncertainties of the gradient. Nonetheless, a successful compensation of the gradient was performed. The measured data was fitted with the linear function

$$\frac{d|B|}{dz} = 0.144\,\frac{\mu\text{G}}{\mu\text{m}\,\text{V}} \cdot U_{\text{thief}} - 0.29\,\frac{\mu\text{G}}{\mu\text{m}} \tag{5.5}$$

leading to zero gradient at $U_{\text{thief}} = 2.05\,\text{V}$.

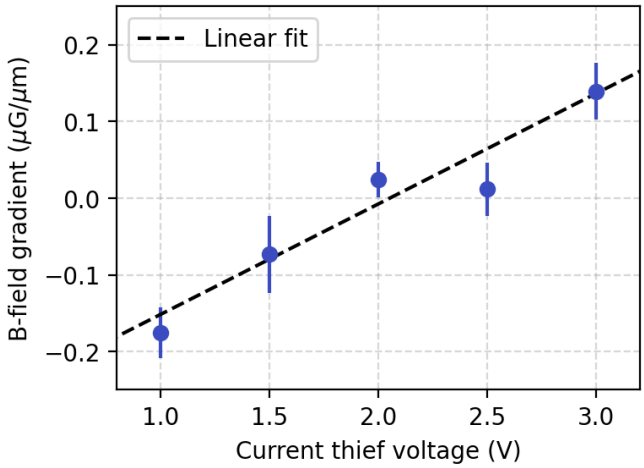

Figure 5.6: Final measurement of the magnetic field gradient at different current thief voltages, following the procedure of Sec. 4.2. A linear fit of the data yields a gradient of zero at a thief voltage of $U_{\text{thief}} = 2.05\,\text{V}$.

After zeroing the B-field gradient, a frequency scan of the E3 transition from $m_J = -1/2$ to $m_J = -1/2$ was performed simultaneously on all ions of the crystal using Rabi spectroscopy. With 36 mW of laser power entering the experimental chamber and a resulting π-pulse duration of $t_\pi = 85\,\text{ms}$, the spectra shown in Fig. 5.7 were measured. The ions are labeled from leftmost to rightmost on the EMCCD image. At each interrogation laser frequency, 100 measurements were performed. The frequency step size of 3 Hz was limited by the 1.5 Hz resolution of the rf frequency source of the doublepass scanning AOM. Each ion's transition is fitted with a Gaussian function to extract the transition center frequency ν_0 and FWHM linewidth.

The fitted transition center frequency of the six central ions in the crystal is identical within the fitting uncertainty of 1 Hz. Only the outer two ions show a red-shift, $\Delta\nu = (-2 \pm 1)\,\text{Hz}$ for the leftmost ion and $\Delta\nu = (-5 \pm 1)\,\text{Hz}$ for the rightmost ion, indicating a smaller AC-Stark shift at both edges of the crystal. A significant residual B-field gradient is not observed, because the transition frequency at each end of the crystal would be shifted in opposite directions. The observed maximum excitation probability of roughly 80% is consistent with the measured decoherence time of $\tau = (190 \pm 27)\,\text{ms}$ [18]. The variance in the maximum excitation probability of the central six ions is likely caused by fitting errors and the broad frequency step size. The AC-Stark shift is so similar for these ions, that there should not be a significant difference in Rabi frequency.

The transition frequency spread shows that the ion crystal is illuminated with a flat section of the shaped beam, which falls off at either side. This agrees well with the AC-Stark shift measurement on the E2 transition, shown in Fig. 5.5. The homogeneity of the laser field can be quantified by using the measured relation $\Delta\nu_{\text{AC,E3}} = (0.66 \pm 0.06)\,\text{Hz}^{-1}\Delta\nu^2_{\text{Fourier}}$ between the absolute AC-Stark shift on the E3 transition $\Delta\nu_{\text{AC,E3}}$ and the Fourier limited linewidth $\Delta\nu_{\text{Fourier}}$ [18]. The average fitted FWHM linewidth of the central six ions is $\Delta\nu_{\text{FWHM}} = (10 \pm 1)\,\text{Hz}$, agreeing well with the Fourier limit of $\Delta\nu_{\text{Fourier}} \approx 0.89/t_\pi = 10.47\,\text{Hz}$ for a rectangular pulse of $t_\pi = 85\,\text{ms}$ duration. This leads to an AC-Stark shift of $\Delta\nu_{\text{AC,E3}} = (66 \pm 7)\,\text{Hz}$. Consequently, the laser intensity deviation across the central six ions is less than $(1.5 \pm 0.2)\%$. The red-shifted transitions of the outer ions correspond to intensity deviations of $(-3.0 \pm 0.4)\%$ and $(-8 \pm 1)\%$. These results agree well with the excitation probabilities calculated in the beginning of this chapter.

The length of the observed flat intensity region is given by the distance between the second and seventh ion from the left, $l = 60\,\mu\text{m}$. By using a higher axial confinement of the crystal, it may be possible to interrogate more than the demonstrated six ions in that region. However, this comes at the cost of higher quadrupole shifts and thus shorter Ramsey dark times in the LLI test, limiting the sensitivity to LV.

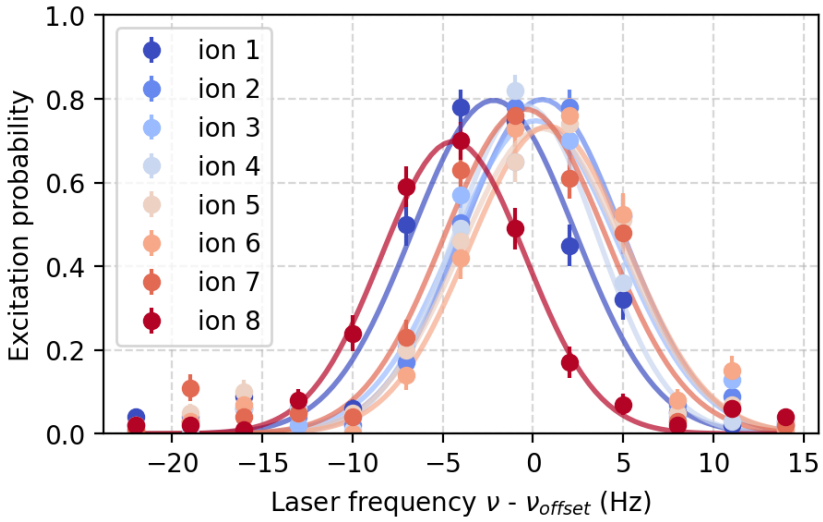

Figure 5.7: Rabi frequency scan of the E3 transition from $m_J = -1/2$ to $m_J = -1/2$ using the shaped line laser profile and an eight ion Coulomb crystal of 80 µm length. A beam power of 36 mW was used, resulting in a π-pulse duration of 85 ms for the central six ions of the crystal. The measured data points are fitted with Gaussian curves.

For the LLI test, a higher excitation probability of 90% would be beneficial, which can be achieved with 50 ms π-pulses. The simulated excitation probabilities in the beginning of this chapter show that the measured laser field intensity variation of $\approx 1.5\%$ across the central six ions is low enough for 50 ms π-pulses. For a 1.7-fold increase in Rabi frequency to reach 50 ms π-pulses, a roughly 3-fold increase in laser power would be necessary, which cannot be accommodated by the currently used laser system. Another method to increase the Rabi frequency is an optimization of the angle between the light's polarization axis and the quantization B-field axis to meet the transition selection rules. At the time of the measurement no large free aperture $\lambda/2$-waveplate was available and the orientation of the polarization axis could only roughly be set by rotating the fiber outcoupler after the polarization maintaining fiber. With the implementation of the waveplate and an optimization of the 467 nm laser power, a significant improvement of the π-pulse duration should be possible.

CHAPTER 6

Conclusion and outlook

Performing experimental tests of local Lorentz invariance is an important cornerstone of searches for new physics beyond the Standard Model. Low energy LLI tests in the combined electron-photon sector, as they are realized in trapped ion experiments, complement a range of lab experiments and astrophysical observations at different energy scales. The LLI test method presented in this thesis has been successfully implemented with a single Yb^+-ion, setting the current most stringent upper bounds to Lorentz violating tensor components for the electron-photon sector in the mid and high 10^{-21}-range [13]. A contribution to this test was made with Ch. 3 of this thesis. The investigation of different dynamical decoupling schemes, lead to the identification of the highly robust UR10 sequence. With this sequence an extension of the coherence time during the rf sequence of about two orders of magnitude was achieved, which was necessary to improve the sensitivity to LV compared to previous experiments. Together with further experimental findings, the main results of Ch. 3 were published in ref. [32].

A high potential of the presented LLI test method lies in its scalability to N ions in a linear Coulomb crystal, resulting in a sensitivity improvement by a factor of $\approx \sqrt{N}$. Chapters 4 and 5 of this thesis work towards an implementation of the test with a ten ion crystal. This would allow a measurement of LV tensor components in the low 10^{-21}-range after the total averaging time for the single-ion test, $\tau = 591\,\mathrm{h}$.

In Ch. 4, the homogeneity of the quantization B-field and the resonant rf-field in the trapping region were measured via simultaneous spectroscopy on a 125 µm Coulomb crystal. The initial B-field gradient was reduced by an order of magnitude to $\leq 0.03\,\mu\mathrm{G}/\mu\mathrm{m}$ by applying a tunable differential current between the B-field coils. Using this method, the gradient can be minimized quickly in the future if long term shifts to the B-field gradient occur. With the demonstrated low gradient, a simultaneous E3 excitation of ions in a 100 µm long crystal with Zeeman shift variations of $\leq 1\,\mathrm{Hz}$ is possible. The measurement of the resonant rf field uniformity showed relative deviations in the π-pulse duration of $< 0.7\%$ over the crystal range of 125 µm. This deviation is well within the UR10's high-fidelity range for rf-pulse duration errors at a dark time of $T_D = 1\,\mathrm{s}$, $-8\% \leq \Delta t/t_\pi \leq 8\%$, as shown in Sec. 3.5. Nonetheless, if the addition of the static gradient-induced pulse duration error should reduce the coherence time compared to the single-ion implementation, using the UR16 sequence with an even higher robustness to pulse duration errors, $-18\% \leq \Delta t/t_\pi \leq 18\%$, could solve the problem.

The most challenging aspect of scaling the LLI test to ten ions is the simultaneous coherent excitation to the $^2F_{7/2}$-state with a large population transfer. In Ch. 5 the successful simulta-

neous excitation of six ions, spaced over $\approx 60\,\mu\text{m}$, with E3 transition frequency shifts of $\leq 1\,\text{Hz}$ is demonstrated. This was achieved by shaping a focused line-shaped top-hat profile with a holographic phaseplate. A $\approx 80\,\mu\text{m}$ long section of the shaped profile has a measured intensity variation of less than $\pm 2\%$ around the average. The phaseplate is designed to produce a uniform intensity over a length of $\approx 150\,\mu\text{m}$. If it is possible to reduce or eliminate the observed spacial noise on the Gaussian input beam, the specified profile will likely be achieved. This would consequently allow the intended simultaneous E3 excitation of ten ions in a $100\,\mu\text{m}$ long crystal.

Bibliography

[1] A. Einstein. Über das Relativitätsprinzip und die aus demselben gezogene Folgerungen. *Jahrbuch der Radioaktivität und Elektronik*, 4, 1907.

[2] A. Einstein and M. Großmann. Entwurf einer verallgemeinerten Relativitätstheorie und einer Theorie der Gravitation. *Zeitschrift für Mathematik und Physik*, 62:225–261, 1913.

[3] V. Alan Kostelecký and Stuart Samuel. Spontaneous breaking of Lorentz symmetry in string theory. *Phys. Rev. D*, 39:683–685, Jan 1989.

[4] Maxim Pospelov and Yanwen Shang. Lorentz violation in Hořava-Lifshitz-type theories. *Physical Review D - Particles, Fields, Gravitation and Cosmology*, 85(10):1–15, 2012.

[5] David Mattingly. Modern Tests of Lorentz Invariance Living Reviews in Relativity. *Living Rev. Relativity*, 8, 2005.

[6] S. Herrmann, A. Senger, K. Möhle, M. Nagel, E. V. Kovalchuk, and A. Peters. Rotating optical cavity experiment testing Lorentz invariance at the 10^{-17} level. *Phys. Rev. D*, 80:105011, Nov 2009.

[7] Ch. Eisele, A. Yu. Nevsky, and S. Schiller. Laboratory Test of the Isotropy of Light Propagation at the 10^{-17} Level. *Phys. Rev. Lett.*, 103:090401, Aug 2009.

[8] M. Schreck. Vacuum Cherenkov radiation for Lorentz-violating fermions. *Phys. Rev. D*, 96:095026, Nov 2017.

[9] A. Albert et al. Constraints on Lorentz Invariance Violation from HAWC Observations of Gamma Rays above 100 TeV. *Phys. Rev. Lett.*, 124:131101, Mar 2020.

[10] T. Pruttivarasin, M. Ramm, S. G. Porsev, I. I. Tupitsyn, M. S. Safronova, M. A. Hohensee, and H. Häffner. Michelson-Morley analogue for electrons using trapped ions to test Lorentz symmetry. *Nature*, 517(7536):592–595, 2015.

[11] Eli Megidish, Joseph Broz, Nicole Greene, and Hartmut Häffner. Entanglement enhanced precision test of local Lorentz invariance. 2018.

[12] Christian Sanner, Nils Huntemann, Richard Lange, Christian Tamm, Ekkehard Peik, Marianna S. Safronova, and Sergey G. Porsev. Optical clock comparison for Lorentz symmetry testing. *Nature*, 567(7747):204–208, 2019.

[13] L.S. Dreissen, CH. Yeh, H.A. Fürst, K.C. Grensemann, and T.E. Mehlstäubler. Improved bounds on Lorentz violation from composite pulse Ramsey spectroscopy in a trapped ion. *Nat. Commun.*, 13, 2022.

[14] R. Shaniv, R. Ozeri, M. S. Safronova, S. G. Porsev, V. A. Dzuba, V. V. Flambaum, and H. Häffner. New Methods for Testing Lorentz Invariance with Atomic Systems. *Physical Review Letters*, 120(10):103202, 2018.

[15] D. Colladay and V. Alan Kostelecký. Lorentz-violating extension of the standard model. *Phys. Rev. D*, 58:116002, Oct 1998.

[16] Albert A. Michelson and M. v. Laue. Die Relativbewegung der Erde gegen den Lichtäther. *Die Naturwissenschaften*, 19(38):779–784, 1931.

[17] R. Lange, A. A. Peshkov, N. Huntemann, Chr Tamm, A. Surzhykov, and E. Peik. Lifetime of the $^2F_{7/2}$ Level in Yb^+ for Spontaneous Emission of Electric Octupole Radiation. *Physical Review Letters*, 127(21):213001, 2021.

[18] H. A. Fürst, C. H. Yeh, D. Kalincev, A. P. Kulosa, L. S. Dreissen, R. Lange, E. Benkler, N. Huntemann, E. Peik, and T. E. Mehlstäubler. Coherent Excitation of the Highly Forbidden Electric Octupole Transition in $^{172}Yb^+$. *Physical Review Letters*, 125(16):163001, 2020.

[19] V. Alan Kostelecký and Charles D. Lane. Constraints on Lorentz violation from clock-comparison experiments. *Phys. Rev. D*, 60:116010, Nov 1999.

[20] M. A. Hohensee, N. Leefer, D. Budker, C. Harabati, V. A. Dzuba, and V. V. Flambaum. Limits on violations of Lorentz symmetry and the Einstein equivalence principle using radio-frequency spectroscopy of atomic dysprosium. *Physical Review Letters*, 111(5):1–5, 2013.

[21] Karsten Pyka. *High-precision ion trap for spectroscopy of Coulomb crystals.* PhD thesis, Leibniz Universität Hannover, 2013.

[22] Tobias Burgermeister. *Development and characterization of a linear ion trap for an improved optical clock performance.* PhD thesis, Leibniz Universität Hannover, 2019.

[23] J. Keller, S. Ignatovich, and S.A. Webster. Simple vibration-insensitive cavity for laser stabilization at the 10^{-16} level. *Appl. Phys. B*, 116:203–210, 2014.

[24] B. Merkel, K. Thirumalai, J. E. Tarlton, V. M. Schäfer, C. J. Ballance, T. P. Harty, and D. M. Lucas. Magnetic field stabilization system for atomic physics experiments. *Review of Scientific Instruments*, 90(4), 04 2019.

[25] N. Huntemann, C. Sanner, B. Lipphardt, Chr Tamm, and E. Peik. Single-Ion Atomic Clock with 3×10^{-18} Systematic Uncertainty. *Physical Review Letters*, 116(6):1–5, 2016.

[26] C. H. Yeh. Excitation of the Forbidden Octupole Transition in $^{172}Yb^+$ Coulomb Crystals. Master's thesis, Leibniz Universität Hannover, 2019.

[27] Jonas Keller. *Spectroscopic characterization of ion motion for optical clock based on Coulomb crystals.* PhD thesis, Leibniz Universität Hannover, 2016.

[28] R. Shaniv, N. Akerman, and R. Ozeri. Atomic Quadrupole Moment Measurement Using Dynamic Decoupling. *Phys. Rev. Lett.*, 116:140801, Apr 2016.

[29] Genko T. Genov, Daniel Schraft, Nikolay V. Vitanov, and Thomas Halfmann. Arbitrarily Accurate Pulse Sequences for Robust Dynamical Decoupling. *Phys. Rev. Lett.*, 118:133202, Mar 2017.

[30] Awad H. Al-Mohy and Nicholas J. Higham. A New Scaling and Squaring Algorithm for the Matrix Exponential. *SIAM Journal on Matrix Analysis and Applications*, 31(3):970–989, 2010.

[31] E. L. Hahn. Spin Echoes. *Phys. Rev.*, 80:580–594, Nov 1950.

[32] C.-H. Yeh, K. C. Grensemann, L. S. Dreissen, H. A. Fürst, and T. E. Mehlstäubler. Robust and scalable rf spectroscopy in first-order magnetic sensitive states at second-long coherence time. *arXiv:2306.01486v1*, 2023.

[33] C. F. Roos, M. Chwalla, K. Kim, M. Riebe, and R. Blatt. 'Designer atoms' for quantum metrology. *Nature*, 443(7109):316–319, 2006.

[34] R. Lange, N. Huntemann, C. Sanner, H. Shao, B. Lipphardt, C. Tamm, and E. Peik. Coherent Suppression of Tensor Frequency Shifts through Magnetic Field Rotation. *Physical Review Letters*, 125(14):143201, 2020.

[35] D. F.V. James. Quantum dynamics of cold trapped ions with application to quantum computation. *Applied Physics B: Lasers and Optics*, 66(2):181–190, 1998.

[36] Claude Cohen-Tannoudji, Bernard Diu, and Franck Laloë. *Band 1 Quantenmechanik*. De Gruyter, Berlin, Boston, 2019.

APPENDIX A

Appendix

A.1 Calculation of the quadrupole shifts for ten ions in a crystal

The electric quadrupole energy shift $\hbar\Delta\nu_{\mathrm{QS}}$ of a Zeeman sublevel $|J, m_J\rangle$ is given by

$$\hbar\Delta\nu_{\mathrm{QS}} = \frac{1}{4}\frac{dE_z}{dz}\Theta(^2F_{7/2})\frac{J(J+1)-3m_J^2}{J(2J-1)}(3\cos^2\beta - 1), \tag{A.1}$$

with the electric field gradient dE_z/dz along the trap axis[1], the quadrupole moment $\Theta(^2F_{7/2})$ and angle β between the quantization axis and the trap axis [33]. The quadrupole moment of the $^2\mathrm{F}_{7/2}$ state of Yb^+ was measured to be $\Theta(^2F_{7/2}) = -0.0297ea_0^2$ with the elementary charge e and Bohr radius a_0 [34]. In Eq. 2.6, κ_{QS} is defined as the component of ν_{QS} that is proportional to m_J^2, the remaining fraction of the quadrupole shift is identical for all Zeeman sublevels. Therefore, κ_{QS} has the form

$$\hbar\kappa_{\mathrm{QS}} = -\frac{1}{4}\frac{dE_z}{dz}\Theta(^2F_{7/2})\frac{3m_J^2}{J(2J-1)}(3\cos^2\beta - 1). \tag{A.2}$$

The electric field gradient dE_z/dz is the sum of the trapping field gradient and the gradient of the electric field generated by other ions in the trap. The trapping field gradient has the form

$$\frac{dE_z}{dz} = \frac{m(2\pi\nu_{\mathrm{ax}})^2}{q}, \tag{A.3}$$

where m is the mass of an ion, q its charge and ν_{ax} the axial secular trapping frequency. The electric field gradient induced by other ions at the location z_i of ion i in a linear crystal of N ions is given by

$$\left.\frac{dE_z}{dz}\right|_{z=z_i} = \sum_{\substack{j=1\\ j\neq i}}^{N}\frac{1}{|z_j - z_i|}\frac{q}{2\pi\epsilon_0}, \tag{A.4}$$

where ϵ_0 is the vacuum permittivity. The coordianates z_i of ion i in a crystal of N ions trapped at ν_{ax} is calculated in Ref. [35]. For the case of $N = 10$ ions, the coordinates are

$$\begin{aligned}[-2.8708, \quad -2.1000, \quad -1.4504, \quad -0.8538, \quad -0.2821, ...\\ ...0.2821, \quad 0.08538, \quad 1.4504, \quad 2.1000, \quad 2.8708] \cdot l\end{aligned} \tag{A.5}$$

with the length scale

$$l = \left(\frac{q^2}{4\pi\epsilon_0 m\nu_{\mathrm{ax}}^2}\right)^{1/3}. \tag{A.6}$$

In the single ion LLI test, κ_{QS} for the specific superposition of Zeeman substates genereated in the Ramsey experiment was measured to be $0.13\,\mathrm{rad\,s^{-1}}$ at an axial secular trapping frequency of $\nu_{\mathrm{ax}} = 266\,\mathrm{kHz}$ [13]. Using the above equations, the measured κ_{QS} for a single ion can be extrapolated for ions in a crystal trapped with the same ν_{ax}. For the case of 10 ions, the result is

$$(\kappa_i) = (0.148,\ 0.174,\ 0.194,\ 0.207,\ 0.214,\ 0.214,\ 0.207,\ 0.194,\ 0.174,\ 0.148)\,\mathrm{rad\,Hz}. \tag{A.7}$$

[1] Here the **z**-direction is defined along the trap axis, in contrast to Chapter 2, where it is defined along the quantization axis.

A.2 Construction of large-J spin matrices

The following derivation is based on ref. [36], $\hbar$ is set to 1. The Zeeman-substates of a spin-J system are eigenstates of the J_z-spin operator

$$J_z \left|J, m_J\right\rangle = m_J \left|J, m_J\right\rangle . \tag{A.8}$$

Thus, the J_z-matrix has the form

$$J_z = \begin{pmatrix} J & & & & \\ & J-1 & & 0 & \\ & & \ddots & & \\ & 0 & & -J+1 & \\ & & & & -J \end{pmatrix} . \tag{A.9}$$

The Zeeman substates can be raised or lowered into neighboring states using the ladder operators

$$J_\pm \left|J, m_J\right\rangle = C_\pm(J, m_J) \left|J, m_J \pm 1\right\rangle , \tag{A.10}$$

where

$$C_\pm(J, m_J) = \sqrt{(J \mp m_J)(J \pm m_J + 1)}. \tag{A.11}$$

Because the ladder operators are defined as

$$J_\pm = J_x \pm i J_y, \tag{A.12}$$

the J_x- and J_y-matrices can be constructed as linear combinations of $J_\pm$:

$$J_x = \frac{J_+ + J_-}{2}, \qquad J_z = \frac{J_+ - J_-}{2i}. \tag{A.13}$$

Using eq. A.10 to obtain the $J_\pm$-matrix representation, J_x and J_y are constructed as

$$J_x = \frac{1}{2} \begin{pmatrix} 0 & C_+(J, J-1) & & & 0 \\ C_-(J, J) & 0 & C_+(J, J-2) & & \\ & \ddots & \ddots & \ddots & \\ & & C_-(J, -J+2) & 0 & C_+(J, -J) \\ 0 & & & C_-(J, -J+1) & 0 \end{pmatrix} \tag{A.14}$$

and

$$J_y = \frac{1}{2i} \begin{pmatrix} 0 & C_+(J, J-1) & & & 0 \\ -C_-(J, J) & 0 & C_+(J, J-2) & & \\ & \ddots & \ddots & \ddots & \\ & & -C_-(J, -J+2) & 0 & C_+(J, -J) \\ 0 & & & -C_-(J, -J+1) & 0 \end{pmatrix} . \tag{A.15}$$